Improved Understanding of Combustor Liner Cooling

Robert Matthew Goodro
St. Catherine's College



A thesis submitted in partial fulfilment of the requirements of the degree of Doctor of Philosophy, Trinity Term, 2009

Department of Engineering Science
University of Oxford
Parks Road, Oxford OX1 3PJ

Abstract

A thesis submitted in partial fulfilment of the requirements of the degree of Doctor of Philosophy at the University of Oxford, Trinity Term, 2009

Robert Matthew Goodro
St. Catherine's College

Improved Understanding of Combustor Liner Cooling

Heat management is an essential part of combustor design, as operating temperatures within the combustor generally exceed safe working temperatures of the materials employed in its construction. Two principal methods used to manage this heat are impingement and film cooling.

Impingement heat transfer refers to jets of impinging fluid delivered by orifices integrated into internal structures in order to remove undesired heat. This mode of heat transfer has a relatively high effectiveness, making it an attractive method of heat management. As such, a considerable number of studies have been done on the subject providing a substantial body of useful knowledge. However, there are innovative cooling configurations being used in gas turbines which generate compressibility and temperature ratio effects on heat transfer which are currently unexplored. Presented here are data showing that these effects have a significant impact on heat transfer and new correlations are presented to account for temperature ratio and Mach number effects for a range of conditions. These findings are significant and can be applied to impinging flows in other areas of a gas turbine engine such as turbine blades and vanes.

Film cooling refers to the injection of coolant onto a surface through an array of sharply angled holes. This is done in a manner that allows the coolant to remain close to the surface where it provides an insulating layer between the hot gas freestream and the cooler surface. In order to improve turbine efficiency, research efforts in film cooling are directed at reducing film cooling flow without decreasing turbine inlet temperatures.

Both impingement cooling and film cooling are heavily utilized in combustor liners. Frequently, cooling air first impinges against the back side of the liner, then the spent impingement fluid passes through film cooling holes. This arrangement combines the convective heat transfer of the impinging jets convection as the coolant passes through the film cooling holes and the benefits that come from having a thin film of cool air between the combustor wall and the combustion products.

In order to improve the understanding of internal cooling in gas turbine engines, the influence of previously unexplored physical parameters such as compressible flow effects and temperature ratio in impingement flows and variable blowing ratio in a film cooling array must be examined. Prior to this work, there existed in the available literature only an extremely limited exploration of compressibility effects in impingement heat transfer and the results of separately examining the effects of Mach number and Reynolds number. The film cooling literature provides no information for a full array of film cooling holes along a contraction at high blowing ratios. Exploring these effects and conditions adds to the body of available data and allows the validation of numerical predictions.

Table of Contents

Title Page i
Abstract ii
List of Figures and Tables vi
Nomenclature x
Acknowledgements xii

Chapter 1 Introduction 1
1.1 Justification for the Present Study 1
1.2 The Gas Turbine Combustion Chamber 6
1.3 Brief Brayton Cycle Overview 6
1.4 Dimensionless Variables 9
1.5 Objectives of the Present Study 11
1.5.1 Impingement Objective 11
1.5.2 Film Cooling Objectives 12
1.6 Literature Survey 13
1.6.1 Impingement Literature Survey 13
1.6.2 Film Cooling Literature Survey 16
1.7 Thesis Organization 21
1.8 The Florschuetz Correlation 22
1.9 List of Publications 24
1.9.1 Conference Publications and Presentations 24
1.9.2 Archival Journal Publications 24

Chapter 2 Experimental Facility and Measurement Techniques for the Impingement Study 25
2.1 Experimental Apparatus 25
2.1.1 Impingement Flow Facility and Impingement Plate 25
2.1.2 Target Plate Test Surfaces 30
2.1.3 Local Impingement Air Pressure and Temperature Measurements 32
2.2 Experimental Procedure 35
2.2.1 Discharge Coefficient Determination 35
2.2.2 Local Recovery Factor Measurement 36
2.2.3 Local Nusselt Number Measurement 37
2.2.4 Determination of Spatially-Averaged Adiabatic Surface Temperature T_{oj}^{*} 41
2.2.5 Experimental Uncertainty Estimates 43
2.2.6 Baseline Nusselt Numbers 44
2.2.7 Impingement Flow Characteristics 46

Chapter 3 Effect of Temperature Ratio on Jet Array Impingement Heat Transfer 48
3.1 Overview 48
3.2 Crossflow-to-Jet Mass Flux Ratio and Discharge Coefficients 48
3.3 Local surface Nusselt Number and Line-Averaged Nusselt Number Variations With Temperature Ratio 50
3.4 Local Area-Averaged Nusselt Number Variations With Temperature Ratio 56

3.5 Local Area-Averaged Nusselt Numbers and the Temperature Ratio Correlation Equation 56
3.6 Summary and Conclusions 61

Chapter 4 Effect of Hole Spacing on Jet Array Impingement Heat Transfer 63
4.1 Overview 63
4.2 Crossflow-to-Jet Mass Flux Ratio and Discharge Coefficients 63
4.3 Local surface Nusselt Number and Line-Averaged Nusselt Number Variations With Hole Spacing 65
4.4 Local Area-Averaged Nusselt Number Variations With Hole Spacing 68
4.5 Summary and Conclusions 72

Chapter 5 Effect of Compressible Flow on Impingement Heat Transfer 75
5.1 Overview 75
5.2 Local surface Nusselt Number and Line-Averaged Nusselt Number Variations With Mach Number 75
5.3 Local Area-Averaged Nusselt Number Variations With Mach Number 78
5.4 Local Area-Averaged Nusselt Numbers and Mach Number Correlation Equations 82
5.5 Summary and Conclusions 87

Chapter 6 Experimental Facility and Measurement Techniques for the Film Cooling Study 90
6.1 Experimental Apparatus 90
6.1.1 Film Cooling Facility 90
6.1.2 Test Surfaces 94
6.1.3 Flow Measurement and Local Surface Temperatures 94
6.2 Experimental Procedure 96
6.2.1 Impulse Response Processing 97
6.2.2 Turbulence Intensity 97
6.2.3 Local and Line-Average Effectiveness 97
6.2.4 Blowing Ratio 98
6.2.5 Experimental Uncertainty Estimates 99
6.2.6 Comparisons to Previous Work 100

Chapter 7 Film Cooling in Gas Turbine Combustors 104
7.1 Overview 104
7.2 Blowing Ratios 104
7.3 Hole Spacing and Blowing Ratio Effects 106
7.4 Varying Contraction Effects 110
7.5 Louvre Experiments 124
7.6 Hole Angle Comparison 127
7.7 Summary and Conclusions 131

Chapter 8 Summary and Conclusions 133
8.1 Summary 133
8.2 Impingement Conclusions 134
8.3 Film Cooling Conclusions 136
8.4 Future Work 137

Appendices

A. Bibliography 139
B. Software Directory 144
C. Uncertainty Analysis 145
D. Impingement Target Plate Iterations 146

List of Figures and Tables

Figure 1.1. Diagram of John Barber's Gas Turbine as presented by Van Der Linden (1988).

Figure 1.2. Diagram of the first commercially viable, industrial gas turbine as presented by Van Der Linden (1988).

Figure 1.3. Siemens SGT5-8000H Gas Turbine (fig. 28 from Diakunchak et al. (2008)).

Figure 1.4 Partial sectional view of a gas turbine engine presented by Abreu and Virenda (1998).

Figure 1.5. Brayton Cycle T-S Diagram for (a) ideal cycle and (b) comparison showing effect of increasing pressure ratio and temperature.

Table 1.1. Geometric parameters used in the Florschuetz correlation (1981).

Figure 2.1. Impingement flow facility.

Figure 2.2. Impingement flow facility test section, including impingement plenum, and impingement channel.

Figure 2.3. Impingement test plate configurations. (a) $X/D = Y/D = 5$. (b) $X/D = Y/D = 8$. (c) $X/D = Y/D = 12$.

Figure 2.4. Target plate cross section.

Figure 2.5. Convection heat power from front side (or impingement side) of the target plate q_{cf} as it varies with $(T_W - T_{oj})$ for $Re_j = 30{,}500$ and $Ma = 0.2$ for hole spacing $X/D, Y/D = 8$.

Figure 2.6. Comparison of baseline Nusselt number data with correlation of Florschuetz et al. (1981) for $Re_j = 34{,}500$, Ma approximately equal to 0, and an array of jets with $X = 5D$, $Y = 4D$, and $Z = 3D$.

Figure 2.7. Characteristic regions in impinging jet flow as presented in Gauntner et al. (1970).

Figure 3.1. (a) crossflow-to-jet mass velocity ratio distribution in streamwise direction determined experimentally (b) crossflow-to-jet mass velocity ratio distribution in streamwise direction predicted using Florscheutz et al. (1981) correlation.

Figure 3.2. Discharge coefficient in streanmwise direction for $Re_j = 18100$, $Ma = 0.2$, and $T_{wa}/T_j = 1.06, 1.25, 1.36, 1.46, 1.58, 1.73$.

Figure 3.3. Spatially-resolved surface Nusselt number distributions for $Re_j = 18000$, $Ma = 0.2$, and $T_{wa}/T_j = 1.06, 1.25, 1.36, 1.46, 1.58$ and 1.73.

Figure 3.4. Local surface Nusselt number variations for $Re_j = 18000$, $Ma = 0.2$, and $T_{wa}/T_j = 1.06, 1.25, 1.36, 1.46, 1.58$ and 1.73. (a) Variations with y/D for $x/D = 32$. (b) Variations with x/D for $y/D = 8$.

Figure 3.5. Surface Nusselt number variations with x/D, which are line-averaged over y/D from -8.0 to +8.0, for $Re_j = 18000$, $Ma = 0.2$, and $T_{wa}/T_j = 1.08, 1.25, 1.37$ and 1.73.

Figure 3.6. Spatially-averaged Nusselt numbers as dependent upon x/D for $Re_j = 18000$, $Ma = 0.2$, and $T_{wa}/T_j = 1.06, 1.25, 1.36, 1.46, 1.58$ and 1.73.

Figure 3.7. Local area averaged Nusselt numbers as dependent upon temperature ratio T_{wa}/T_j for $Re_j = 18000$ and $Ma = 0.2$.

Figure 3.8. Nusselt numbers ratio data at specific x/d locations correlated with respect to temperature ratio, T_{wa}/T_j.

Figure 4.1. (a) Crossflow-to-jet mass velocity ratio with row number for hole spacings of 5*D*, 8*D*, and 12*D* and (b) discharge coefficient coefficient varations with Re_j for hole spacings of 5*D*, 8*D*, and 12*D* at constant Mach number 0.2.
Figure 4.2. Spatially resolved distributions of surface Nusselt number for *Ma* = 0.2 with hole spacings and Re_j values of: (a) 5*D* and Re_j = 17300, (b) 5*D* and Re_j = 30000, (c) 5*D* and Re_j = 60000, (d) 8*D* and Re_j = 17300, (e) 8*D* and Re_j = 30000, (f) 8*D* and Re_j = 60000, (g) 12*D* and Re_j = 17300, (h) 12*D* and Re_j = 30000, (i) 12*D* and Re_j = 60000
Figure 4.3. Local surface Nusselt number variations for *Ma* = 0.2 and Re_j values of 17300, 30000, and 60000: (a) hole spacing 5*D* spanwise variations, (b) hole spacing 5*D* lengthwise variations, (c) hole spacing 8*D* spanwise variations, (d) hole spacing 8*D* lengthwise variations, (e) hole spacing 12*D* spanwise variations, (f) hole spacing 12*D* lengthwise variations.
Figure 4.4. Surface Nusselt number variations which are line averaged over y/D for one hole spacing in either direction from the origin, for constant Mach number 0.20 and (a) hole spacing 5*D* Re_j = 17300, 30000, and 60000, (b) hole spacing 8*D* Re_j = 17300, 30000, and 60000, (c) hole spacing 12*D* Re_j = 17300, 30000, and 60000.
Figure 4.5. Hole spacing *X/D* = *Y/D* = 5 comparison of area average Nusselt numbers with correlation of Florschuetz et al. (1981) for *Ma* = 0.17, and Re_j = 17300, 30000, and 59000.
Figure 4.6. Hole spacing *X/D* = *Y/D* = 8 comparison of area average Nusselt numbers with correlation of Florschuetz et al. (1981) for *Ma* = 0.2, and Re_j = 17300, 30000, and 59000.
Figure 4.7. Hole spacing *X/D* = *Y/D* = 12 comparison of area average Nusselt numbers with correlation of Florschuetz et al. (1981) for *Ma* = 0.2, and Re_j = 17300, 30000, and 59000.
Figure 5.1. Spatially resolved distributions of surface Nusselt number for Re_j = 30000 with hole spacings and *Ma* values of: (a) 5*D* and *Ma* = 0.09, (b) 5*D* and *Ma* = 0.17, (c) 5*D* and *Ma* = 0.30, (d) 5*D* and *Ma* = 0.38, (e) 8*D* and *Ma* = 0.20, (f) 8*D* and *Ma* = 0.35, (g) 8*D* and *Ma* = 0.45, (h) 12*D* and *Ma* = 0.10, (i) 12*D* and *Ma* = 0.17, (j) 12*D* and *Ma* = 0.38, (k) 12*D* and *Ma* = 0.45
Figure 5.2. Local surface Nusselt number variations for Re_j = 30,000 and *Ma* values of 0.1, 0.2, 0.35, and 0.45: (a) hole spacing 5*D* spanwise variations, (b) hole spacing 5*D* lengthwise variations, (c) hole spacing 8*D* spanwise variations, (d) hole spacing 8*D* lengthwise variations, (e) hole spacing 12*D* spanwise variations, (f) hole spacing 12*D* lengthwise variations.
Figure 5.3. Surface Nusselt number variations which are line averaged over y/D for one hols spacing in either direction from the origin for constant Reynolds number 30000 and (a) hole spacing 5*D* *Ma* = 0.09, 0.17, 0.30, and 0.38, (b) hole spacing 8*D* *Ma* = 0.20, 0.35, 0.45, and 0.59, (c) hole spacing 12*D* *Ma* = 0.10, 0.17, 0.38, and 0.45.
Figure 5.4. Hole spacing *X/D* = *Y/D* = 5 comparison of area average Nusselt numbers with correlation of Florschuetz et al. (1981) for Re_j = 30,000 and *Ma* values of 0.1, 0.17, 0.30, and 0.38.

Figure 5.5. Hole spacing $X/D = Y/D = 8$ comparison of area average Nusselt numbers with correlation of Florschuetz et al. (1981) for $Re_j = 30{,}000$ and *Ma* values of 0.1, 0.2, 0.35, 0.45, and 0.59.
Figure 5.6. Hole spacing $X/D = Y/D = 12$ comparison of area average Nusselt numbers with correlation of Florschuetz et al. (1981) for $Re_j = 30{,}000$ and *Ma* values of 0.1, 0.2, 0.35, 0.38, and 0.45.
Figure 5.7. Nusselt number correlation with Mach number for hole spacing $X/D = 5$, $Re_j = 30{,}000$ and Ma values of 0.11, 0.20, 0.30, and 0.38.
Figure 5.8. Nusselt number correlation with Mach number for hole spacing $X/D = 8$, $Re_j = 30{,}000$ and Ma values of 0.11, 0.20, 0.35, and 0.45.
Figure 5.9. Nusselt number correlation with Mach number for hole spacing $X/D = 12$, $Re_j = 30{,}000$ and Ma values of 0.11, 0.20, 0.35, 0.38, and 0.45.
Figure 5.10. Comparison between Nusselt number correlations for hole spacings of 5, 8, and 12.
Figure 6.1. Overview of film cooling test facility.
Figure 6.2. Film cooling test section.
Figure 6.3. Local effectiveness comparison plot.
Figure 6.4. Spatially averaged effectiveness comparison plot.
Figure 7.1. Blowing ratio progression with *x/D* for different contraction ratios, calculated on the basis of static pressure ratios..
Figure 7.2. Spatially resolved effectiveness at blowing ratios for hole spacing $X/D = 6$, $Y/D = 3$, $Cr = 4$, and (a) $BR = 2.0$, *x/D* from 0 to 50, (b) $BR = 2.0$, *x/D* from 46 to 95, (c) $BR = 5.0$, *x/D* from 0 to 50, (d) $BR = 5.0$, *x/D* from 46 to 95, (e) $BR = 10.0$, *x/D* from 0 to 50, and (f) $BR = 10.0$, *x/D* from 46 to 95.
Figure 7.3. Spatially resolved effectiveness at blowing ratios for hole spacing $X/D = 6$, $Y/D = 5$, $Cr = 4$, and (a) $BR = 2.0$, *x/D* from 0 to 50, (b) $BR = 2.0$, *x/D* from 46 to 95, (c) $BR = 5.0$, *x/D* from 0 to 50, (d) $BR = 5.0$, *x/D* from 46 to 95, (e) $BR = 10.0$, *x/D* from 0 to 50, and (f) $BR = 10.0$, *x/D* from 46 to 95.
Figure 7.4. Spatially resolved effectiveness at blowing ratios for hole spacing $X/D = 6$, $Y/D = 7$, $Cr = 4$, and (a) $BR = 2.0$, *x/D* from 0 to 51, (b) $BR = 2.0$, *x/D* from 46 to 94, (c) $BR = 5.0$, *x/D* from 0 to 51, (d) $BR = 5.0$, *x/D* from 46 to 94, (e) $BR = 10.0$, *x/D* from 0 to 51, and (f) $BR = 10.0$, *x/D* from 46 to 94.
Figure 7.5. Variations of spatially averaged effectiveness at different hole spacings for $BR = 2.0$.
Figure 7.6. Variations of spatially averaged effectiveness at different hole spacings for $BR = 5.0$.
Figure 7.7. Variations of spatially averaged effectiveness at different hole spacings for $BR = 10.0$.
Figure 7.8. Comparison of spatially averaged effectiveness at different blowing ratios for hole spacing $X/D = 6$, $Y/D = 3$.
Figure 7.9. Comparison of spatially averaged effectiveness at different blowing ratios for hole spacing $X/D = 6$, $Y/D = 5$.
Figure 7.10. Comparison of spatially averaged effectiveness at different blowing ratios for hole spacing $X/D = 6$, $Y/D = 7$.
Figure 7.11. Comparison of spatially averaged effectiveness values for $X/D = 6$, $Y/D = 5$, blowing ratios 2.0, 5.0, and 10.0, and contraction ratios 1, 3, 4, and 5.

Figure 7.12. Spatially resolved effectiveness at different contraction ratios and blowing ratios for hole spacing X/D = 18, Y/D = 5 and (a) BR = 2.0, Cr = 1, x/D from 0 to 41 (b) BR = 2.0, Cr = 1, x/D from 40 to 89 (c) BR = 5.0, Cr = 1, x/D from 0 to 41 (d) BR = 5.0, Cr = 1, x/D from 40 to 89 (e) BR = 10.0, Cr = 1, x/D from 0 to 41 (f) BR = 10.0, Cr = 1, x/D from 40 to 89.

Figure 7.13. Spatially resolved effectiveness at different contraction ratios and blowing ratios for hole spacing X/D = 18, Y/D = 5 and (a) BR = 2.0, Cr = 4, x/D from 0 to 50 (b) BR = 2.0, Cr = 4, x/D from 45 to 95 (c) BR = 5.0, Cr = 4, x/D from 0 to 50 (d) BR = 5.0, Cr = 4, x/D from 45 to 95 (e) BR = 10.0, Cr = 4, x/D from 0 to 50 and (f) BR = 10.0, Cr = 4, x/D from 45 to 95.

Figure 7.14. Spatially averaged effectiveness for X/D = 18, Y/D = 5, blowing ratios 2.0, 5.0, and 10.0, and a contraction ratio of 1.

Figure 7.15. Spatially averaged effectiveness for X/D = 18, Y/D = 5, blowing ratios 2.0, 5.0, and 10.0, and a contraction ratio of 4.

Figure 7.16. Spatially resolved effectiveness for X/D = 6, Y/D = 5 and Cr = 4 with the inclusion of a louver operating at BR = 1 and film cooling blowing ratio of (a) 2.0 from x/D = 0 to x/D = 50, (b) 2.0 from x/D = 45 to x/D = 95, (c) 5.0 from x/D = 0 to x/D = 50, (d) 5.0 from x/D = 45 to x/D = 95, (e) 10.0 from x/D = 0 to x/D = 50, and (f) 10.0 from x/D=45 to x/D=95.

Figure 7.17. Spatially averaged effectiveness for X/D = 6, Y/D = 5 and Cr = 4 with the inclusion of a louver operating at BR = 1.

Figure 7.18. Spatially resolved effectiveness values for X/D = 6, Y/D = 5 and Cr = 1 for a test surface with hole inclination angle θ = 30º and (a) BR=2.0, x/D from 0 to 41 (b) BR=2.0, x/D from 40 to 89 (c) BR=5.0, x/D from 0 to 41 (d) BR=5.0, x/D from 40 to 89 (e) BR=10.0, x/D from 0 to 41 (f) BR=10.0, x/D from 40 to 89.

Figure 7.19. Spatially resolved effectiveness values for X/D=6, Y/D=5 and Cr=4 for a test surface with hole inclination angle θ=30º and (a) BR=2.0, x/D from 0 to 41 (b) BR=2.0, x/D from 40 to 89 (c) BR=5.0, x/D from 0 to 41 (d) BR=5.0, x/D from 40 to 89 (e) BR=10.0, x/D from 0 to 41 (f) BR=10.0, x/D from 40 to 89.

Figure 7.20. Spatially averaged effectiveness comparison plot for a test surface with hole inclination angle θ=30º, hole spacing X/D=6, Y/D=5 and contraction ratios of 1 and 4.

Table B.1. Listing of data analysis programs and their uses for the impingement study.

Table B.2. Listing of data analysis programs and their uses for the film cooling study.

Table C.1 Uncertainty analysis result.

Figure D.1. First Target Plate Iteration.

Figure D.2. Pressure Damaged Target Plate.

Figure D.4. Target Plate for Use with High Speed Impingement Jets.

Figure D.5 Target Plate Properly Mounted on Impingement Plenum.

Nomenclature

A	impingement hole area
A_{cross}	exit channel cross-sectional area
A_{ht}	heat transfer area on the target plate
BR	film cooling blowing ratio
c_a	impingement air flow sonic velocity
C_D	discharge coefficient
D	diameter of an individual impingement hole
f_s	sampling frequency
G_c	crossflow mass velocity or crossflow mass flux
G_j	jet mass velocity or jet mass flux
h_f	film cooling heat transfer coefficient
h_{loss}	heat transfer coefficient to account for convection and radiation loss from back side of target plate
k	ratio of specific heats
$\dot{m}$	impingement air mass flow rate
$\dot{m}_c$	crossflow air mass flow rate
M_a	impingement air flow Mach number, where Mach number is the ratio of absolute velocity to the speed of sound for a given medium
M_i	impingement air flow ideal Mach number
Nu	local Nusselt number, the ratio of convective to conductive heat transfer normal to the test surface
$\overline{Nu}$	line-averaged Nusselt number
$\overline{\overline{Nu}}$	spatially-averaged Nusselt number
$\overline{\overline{Nu}}_{cp}$	constant property spatially-averaged Nusselt number
Nu_f	Nusselt number predicted by Florschuetz et al. [5]
P_a	impingement air static pressure
P_c	film cooling coolant source static pressure
P_{oj}	impingement air stagnation pressure
P_∞	film cooling freestream static pressure
Q	total power provided to the thermofoil heater
q_f	film-cooled surface heat flux
q_{rf}	radiation heat flux from front side (or impingement side) of the target plate
q_{rb}	radiation heat flux from back side of the target plate
q_{cf}	convection heat flux from front side (or impingement side) of the target plate
q_{cb}	convection heat flux from back side of the target plate
R	ideal gas constant
Re	Reynolds number, a dimensionless number that gives a measure of the ratio of inertial forces to viscous forces
Re_j	impingement air flow Reynolds number
Re_{fc}	film cooling Reynolds number
t	time
$T_{ambient}$	ambient static temperature
T_{ave}	mass-averaged temperature exiting the test section.
T_{aw}	adiabatic wall temperature

T_b local temperature on the back surface of the polystyrene target plate
T_c coolant temperature
T_W local target surface temperature on the surface of the heater adjacent to the cooling fluid
Ti impingement air ideal static temperature
T_j impingement air static temperature
T_{oj} impingement air stagnation temperature
T_{oj}* corrected impingement air stagnation temperature to give zero spatially-averaged surface heat flux
T_{tc} local thermocouple temperature between the heater and the polystyrene target plate
T_∞ freesteam air stagnation temperature
u_a impingement air velocity
u_c crossflow velocity
u_{fc} film cooling coolant exit velocity
u_i impingement air ideal velocity
u_{jet} jet air velocity
u_∞ film cooling freestream velocity
x streamwise coordinate
y spanwise coordinate
z normal coordinate
X streamwise distance between centerlines of adjacent impingement holes
Y spanwise distance between centerlines of adjacent impingement holes
Z distance between target plate and impingement hole plate

Greek symbols

α air thermal conductivity
β flow distribution parameter
ρ_a impingement air static density
ρ_c film cooling coolant density
ρ_i impingement air ideal static density
ρ_∞ film cooling freestream density
μ absolute viscosity
η_{aw} film-cooling effectiveness
$\bar{\eta}$ spatially-averaged effectiveness
θ film cooling hole angle of inclination relative to the test surface
σ Boltzman constant
ε_f emissivity of the front surface of the target plate
ε_{inf} emissivity of a plate located opposite to the target plate

Acknowledgements

Upon the completion of this work I wish to acknowledge the people who have assisted in making this possible. To begin, I wish the thank Prof. Phil Ligrani and Dr. David Gillespie for each of their efforts in the role of supervisor. Their guidance and support have been of great value throughout my time at the University of Oxford.

The support of the technical staff at Osney Laboratory has been immeasurably important throughout this project and I would like to extend special thanks to Dave Mountain, Gerald Walker, Trevor Godfrey, and Paul Cox for their particular efforts in construction and support of my test facilities.

I also wish to express gratitude to my wife Christy. Without her support and encouragement, my educational goals; of which this work is an essential part, would not have come to fruition.

The research project reported here was sponsored by Solar Turbines Inc. I would like to acknowledge Dr. Hee-Koo Moon and Mike Fox of Solar Turbines Inc. for their guidance and suggestions throughout this research effort.

Chapter 1

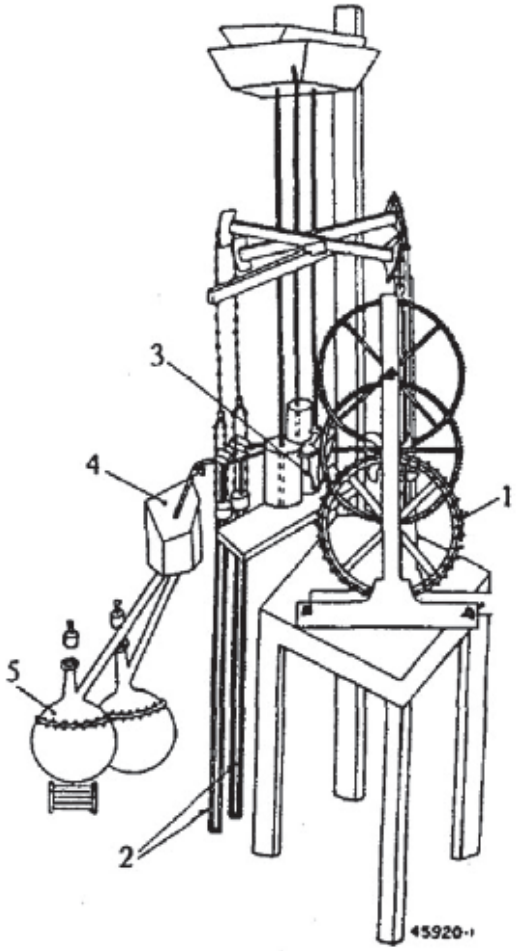
Introduction

1.1 Justification for the Present Study

A casual examination of gas turbine history reveals that the concept of a gas-driven rotary device is many centuries old. As early as 150 AD, the Egyptian philosopher and mathematician Hero, made a device that rotated above a pot of boiling water. The more contemporary inventor, Leonardo da Vinci, sketched a device intended to use hot air rising from a fireplace to power a roasting spit in 1500. The first patent for an actual gas turbine was awarded to John Barber in 1791. Figure 1.1 shows a diagram of his engine which consisted of a chain-driven gas compressor, a combustion chamber and a turbine. Unfortunately it did not generate sufficient power to drive the compressor. It was not until 1903 that a gas turbine was able to generate more power than was required to run its own internal processes. It was developed by a Norwegian inventor by the name of Aegidius Elling and produced a net output of 8 kW (Johnson, 1985).

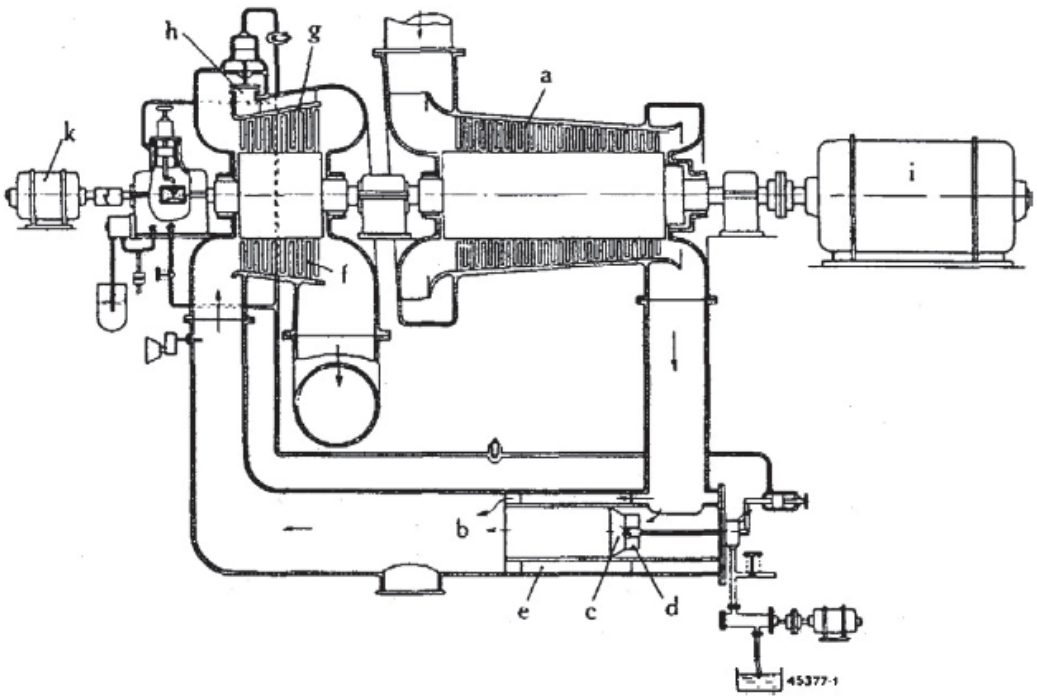
The first world's first commercial gas turbine was built by a Swiss development company, Brown, Boveri & Cie (BBC) in 1938. It went into operation in 1939 and remained in service until 2002. It operated at an efficiency of 17.4% and had a net power output of 4 MW. It operated at a rotational speed of 3000 rpm and turbine inlet temperature of 550ºC (Van Der Linden, 1988). Figure 1.2, the facility layout, is provided for comparison with fig. 1.1.

Design improvements after 1939 have resulted in an efficiency increase from 17.4% to 40% or higher in the simple Brayton cycle configuration used in the 1939



1. Turbine
2. Gas and air compressor
3. Combustion chamber
4. Receiver
5. Gas producer

Figure 1.1. Diagram of John Barber's Gas Turbine as presented by Van Der Linden (1988).



. Diagram of the simplest form of combustion turbine plant. With reaction type gas turbine and axial compressor for oil fuel, and with excess air cooling.

a. Axial compressor
b. Combustion chamber
c. Combustion nozzle
d. Burner
e. Cooling-air jacket
f. Gas-turbine blading
g. Gas turbine
h. Safety valve
i. Generator
j. Starting motor

Figure 1.2. Diagram of the first commercially viable, industrial gas turbine as presented by Van Der Linden (1988).

design. Modifications to the basic thermodynamic cycle such as inter-cooling, which uses a heat exchanger to cool compressor gas during compression, and recuperation, where a heat exchanger uses exhaust gas to preheat compressed gas before it enters the combustor, serve to improve efficiency even further. The improvement in efficiency for a simple Brayton cycle comes from improved design, increased pressure ratio, and higher turbine inlet temperatures. Current gas turbine inlet temperatures are several hundred degrees higher than the 550ºC used in 1939 (Bhargava et al., 2008). Figure 1.3 shows the Siemens SGT5-8000H gas turbine, a modern industrial gas turbine designed to produce 340 MW at an efficiency of 39%. It is optimized to work in a combined cycle power plant, where the exhaust heat is used to generate steam for power production through a steam turbine. The combined cycle operates at a thermal efficiency greater than 60% for a total power output of 530 MW (Diakunchak et al., 2008).

Even with the development of thermal barrier coatings and new, innovative materials capable of withstanding high heat for extended run times, the drive to increase efficiency by increasing turbine inlet temperature has created a situation where temperatures in the combustor and turbine far exceed safe working temperatures for the materials involved. Impingement heat transfer, full-coverage film cooling, and slot cooling (which is another form of film cooling) are the primary cooling methods used to protect combustor liners and turbine blades. In air cooled gas turbines such as the Siemens SGT5-8000H, the coolant is extracted from the compressor and causes a decrease in efficiency by increasing the compressor work load. Improvements in cooling design can result in reduced coolant flow which causes an overall increase in cycle efficiency. The present work serves to improve the

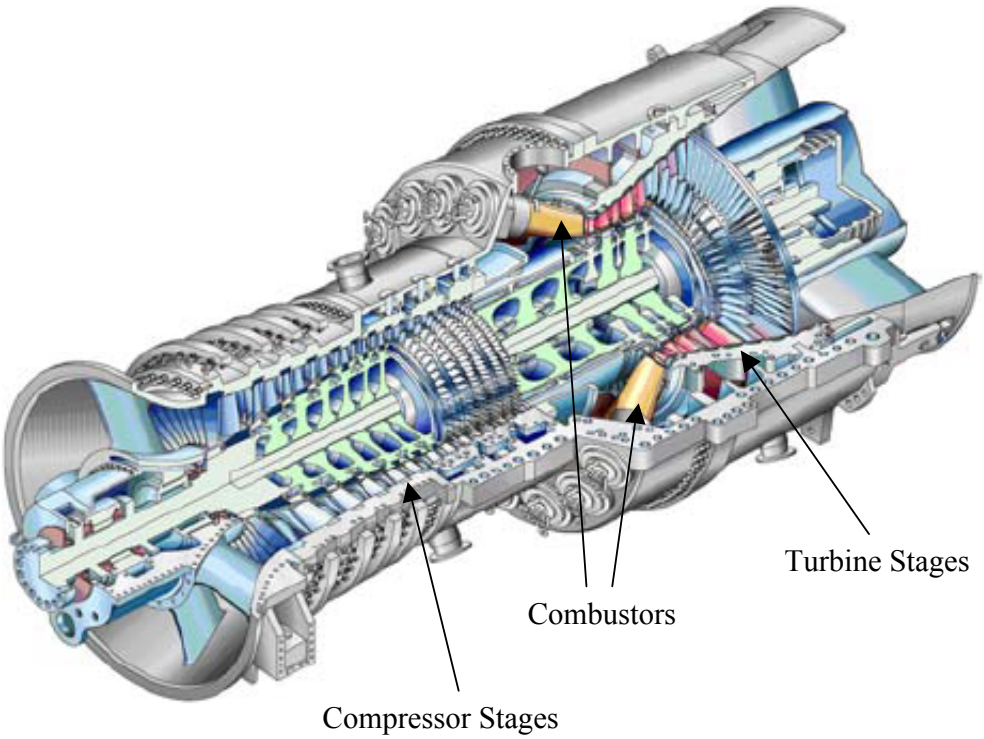


Figure 1.3. Siemens SGT5-8000H Gas Turbine (fig. 28 from Diakunchak et al. (2008)).

understanding of flow phenomena present in cooling flows which in turn allows for improved modeling and design.

1.2 The Gas Turbine Combustion Chamber

Figure xx is a partial sectional view of a gas turbine engine which focuses on the liner of an annular combustion chamber. In this case, the entire liner is protected by both impingement and film cooling (Abreu & Virenda, 1998). The majority of the liner's internal surface area is at a contraction ratio of 1 (no contraction) and therefore has only a small static pressure gradient. Roughly the last third of the combustion chamber's length is sharply angled with a strong pressure gradient which affects the film cooling blowing ratio. This design highlights the importance of understanding both impingement cooling and the effect of a contraction on full-coverage film cooling.

1.3 Brief Brayton Cycle Overview

Simple cycle gas turbines operate through a thermodynamic process known at the Brayton cycle. It is the cycle originally proposed in John Barber's 1791 patent application, but is named after the American inventor George Brayton who developed it for use with separate piston compressors and expanders. The ideal Brayton cycle has four phases: isentropic compression, isobaric heat addition, isentropic expansion, and isobaric heat rejection. It is represented in fig. 1.5a. Due to second-law losses, neither the compression nor expansion process is isentropic. Losses in the compressor and expander associated with increasing entropy represent working inefficiencies. As previously mentioned, increasing the pressure ratio and turbine inlet temperature improves efficiency. This is demonstrated in fig. 1.5b. The improvement in efficiency

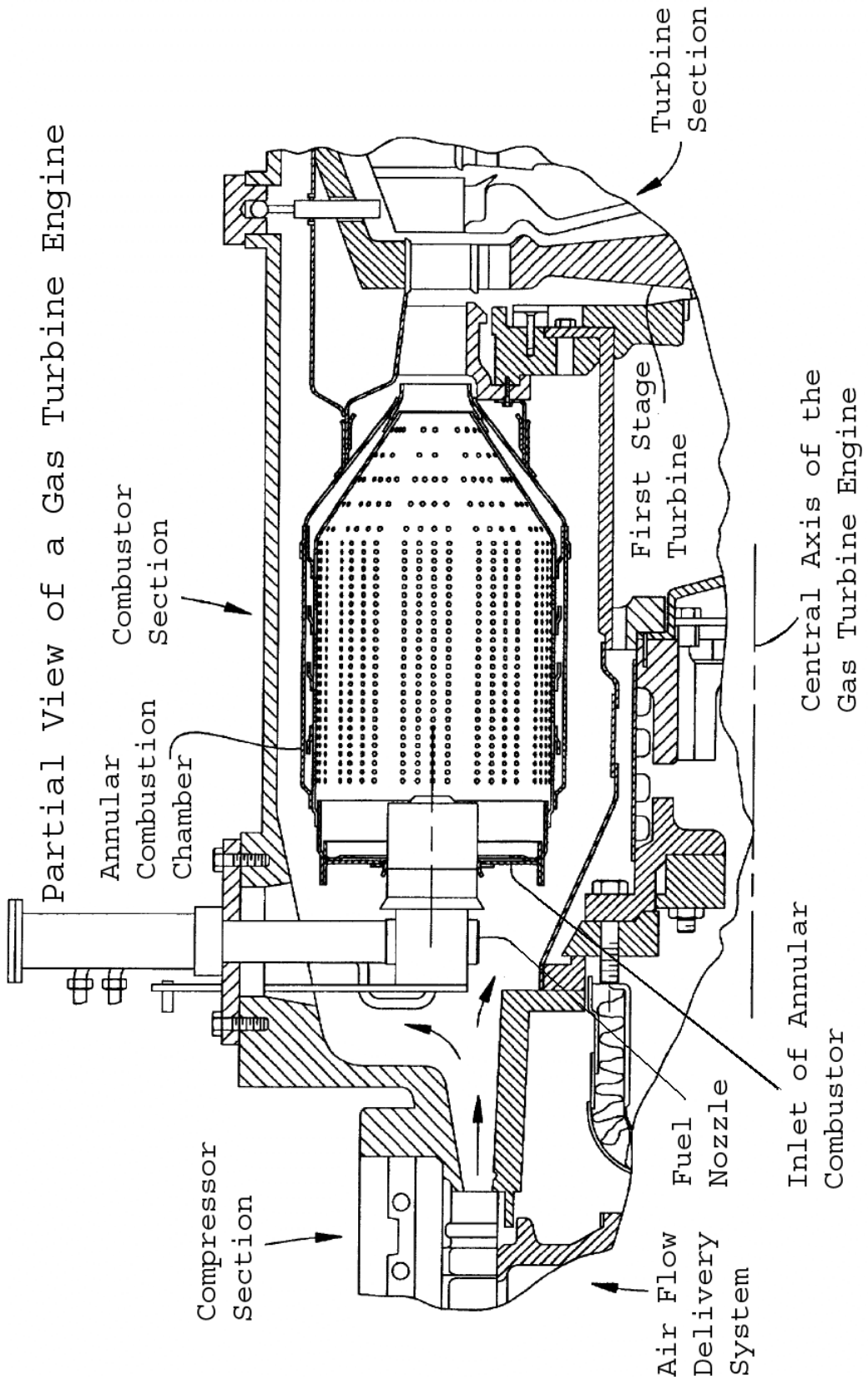
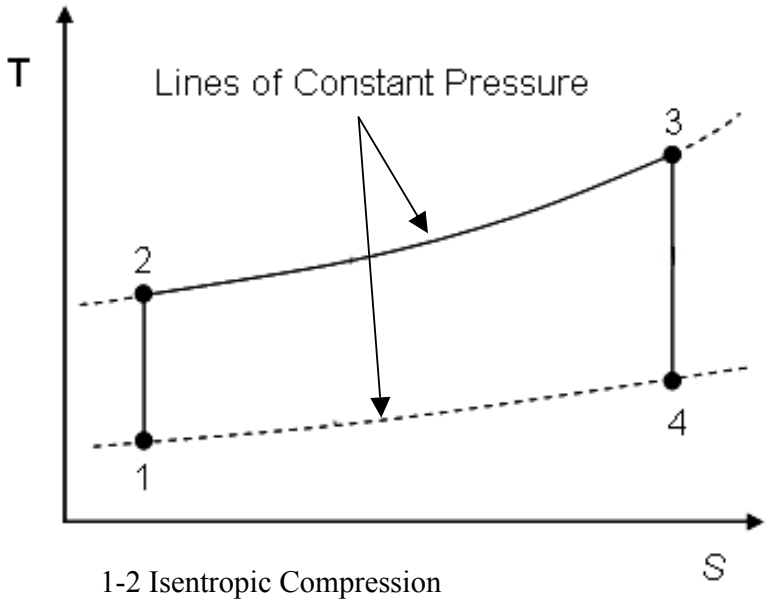


Figure 1.4 Partial sectional view of a gas turbine engine presented by Abreu and Virenda (1998).

(a)



1-2 Isentropic Compression
2-3 Isobaric Heat Addition
3-4 Isentropic Expansion
4-1 Isobaric Heat Rejection

(b)

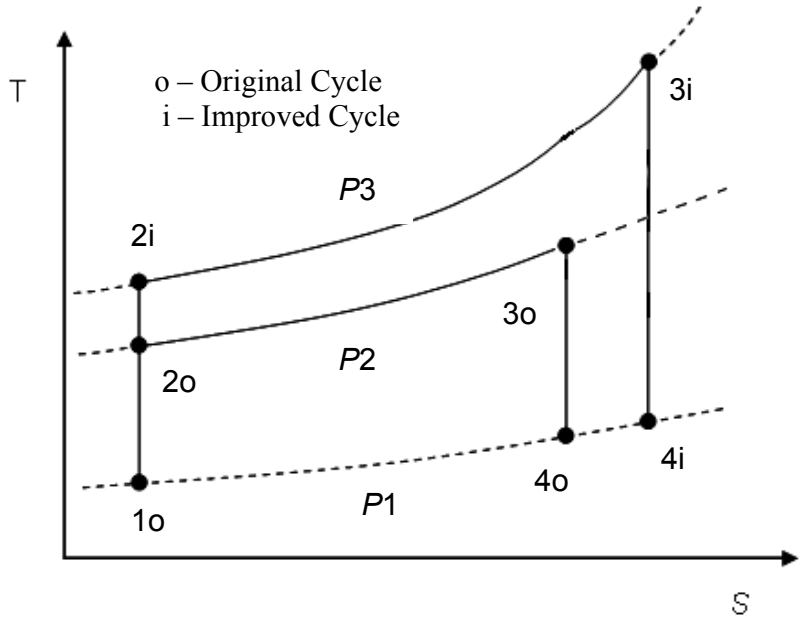


Figure 1.5. Brayton Cycle T-S Diagram for (a) ideal cycle and (b) comparison showing effect of increasing pressure ratio and temperature.

comes from in increase in ratio between the distance from point 1 to 2 and from point 3 to 4. The net work out is the difference between the two lengths.

1.4 Dimensionless Variables

The dimensionless variables used in the present study are: Reynolds number (*Re*), Mach number (*Ma*), Nusselt number (*Nu*), discharge coefficient (C_D), blowing ratio (*BR*), and effectiveness (η). Because the test facilities used in the present study are not to industrial gas turbine scale and do not operate at normal running conditions, it is necessary to frame results in terms of dimensionless variables so that dimensional analysis may be used to apply the results to as wide a range of turbine configurations and operating conditions as possible. Dimensional analysis is necessary when applying data from a system at one scale to a design problem at a different scale. For the impingement data, in systems with incompressible flow, matching the Reynolds number in the model to the Reynolds number in an actually combustor liner will give the same Nusselt numbers for the two systems. When compressibility effects are present, it is necessary to match both the Reynolds number and Mach number to get equivalent Nusselt numbers. For film cooling flows, matching the blowing ratio is required to have the same effectiveness values in the modal and an actual combustor liner.

Reynolds number is a measure of the ratio between inertial forces and viscous forces. It is a non-dimensional measure of velocity. For impingement jets, Reynolds numbers takes the form

$$\mathrm{Re}_j = \rho_a u_a D / \mu \tag{1.1}$$

where ρ_a is the impingement air static density, u_a is the impingement air velocity, D is the impingement jet diameter and μ is the absolute viscosity. Mach number, like

Reynolds number, is a measure of velocity. It is the speed of an object moving through any fluid, divided by the speed of sound in that medium. It takes the form

$$M_a = u_a / c_a \tag{1.2}$$

where u_a is the impingement air velocity and c_a is the impingement air flow sonic velocity. Nusselt number is the ratio of convective heat transfer to conduction normal to the boundary. The convection and conduction flows are parallel to each other and perpendicular to the bulk flow. Because the components of the Nusselt number cannot be determined directly here, as in the case of the Reynolds number, it must be determined through an analysis involving radiation, heat flux, thermocouple temperature and a 1-D conduction analysis. This is explained in more detail in chapter 2. The discharge coefficient is the ratio of actual mass flux to ideal mass flux across a hole or nozzle and takes the form

$$C_D = \rho_a u_a / \rho_i u_i \tag{1.3}$$

where ρ_a is the actual air static density, u_a is the actual air velocity, ρ_i is the ideal air static density, u_i is the ideal air velocity. In the impingement study the discharge coefficient is the ratio of mass flux across the impingement plate used to generate the impinging jets. In the film cooling study, it is the ratio across the film cooling test surface and the film cooling exit velocity is used instead of the impingement jet velocity. Blowing ratio is the ratio of film cooling mass flux to freesteam mass flux. It is represented mathematically as

$$B_R = \rho_c u_{fc} / \rho_\infty u_\infty \tag{1.4}$$

where ρ_c is the coolant static density, u_{fc} is the film cooling exit velocity, ρ_∞ is the freestream static density, u_∞ is the freestream velocity. Film cooling effectiveness is a measure of dimensionless adiabatic wall temperature. It is defined as

$$\eta_{aw} = (T_{aw} - T_\infty)/(T_c - T_\infty) \quad (1.5)$$

where T_{aw} is the adiabatic wall temperature, T_∞ is the freestream temperature, and T_c is the coolant temperature.

1.5 Objectives of the Present Study

The present objectives are described in two parts, impingement and film cooling.

1.5.1 Impingement Objectives

Nusselt number can be represented as a function of Reynolds number, Mach number, temperature ratio, and Prandtl number. Roughly 30 years ago, a significant volume of work performed by Florschuetz et al. (1981) culminated in the development a powerful correlation used to predict average Nusselt number distributions for impingement flows based on hole spacing and Reynolds number. This correlation, while extremely useful, neglects the contributions of Mach number and temperature ratio to impingement heat transfer. In 2001 Brevet et al. challenged the validity of neglecting Mach number when they published their findings on the effect compressibility plays on the heat transfer characteristics of an impinging jet establishing that Mach number has a significant effect on Nusselt number for a single compressible jet.

The present work on impingement has several objectives. The first of which is to provide data on the separate effects of Mach number and Reynolds number for an array of impinging jets in the form of discharge coefficients, and local and spatially-averaged Nusselt numbers. The second objective is to quantify the effect of changing temperature ratio at a set value of Mach number and Reynolds number and address the results in terms of the effects of temperature-dependent fluid properties, as they affect local and global turbulent transport in the flow field created by the array of impinging jets. The effect of temperature ratio on crossflow-to-jet mass velocity ratio and discharge coefficient is also examined. The third objective is providing new spatially-resolved impingement heat

transfer data on the effects of hole spacing at different Reynolds number and Mach numbers including compressibility effects. Note that no other existing investigation considers the effects of temperature ratio on jet array impingement heat transfer in any depth. As such, the present results represent a new contribution to the archival literature as the effects of temperature ratio on jet array impingement heat transfer are illustrated. The hole spacing investigation is unique and different from data given in other recent studies because the flow conditions and configurations employed are *new*. As such, the data obtained are important because they illustrate the dependence of local and spatially-averaged Nusselt numbers on jet Mach number and jet Reynolds number, for different jet spacings.

1.5.2 Film Cooling Objectives

There is a need for design engineers to have film cooling effectiveness data for a wide range of film cooling arrangements. With this in mind, a unique facility was designed and assembled at the University of Oxford Thermo-Fluids Laboratory to obtain experimental data over the entire length of the contraction at the combustor's exit for full coverage film cooling as the following experimental parameters are changed: blowing ratio, film cooling jet Reynolds number, spanwise and streamwise film cooling hole spacing, film cooling hole inclination angle, and contraction ratio. The effect of a louver prior to the contraction of a fully film cooled combustor liner is also explored.

Careful review of available film cooling literature reveals that no published data exists considering full-coverage film cooling through a contraction. The free-stream pressure drop through such a contraction combined with a constant pressure cooling fluid source results causes a change in blowing ratio along the length of the contraction due to the varying mass flux in both the freestream and the coolant flow. By varying the previously mentioned variables, their effects in such a condition will be explored. This will provide information of interest to design engineers and scholars alike while adding to the body of film cooling knowledge.

1.6 Literature Survey

Like the objectives, the survey of available literature is described in separate sections for impingement and film cooling.

1.6.1 Impingement Literature Survey

A significant number of papers on impingement cooling are available. Most existing investigations address low Mach number flows with relatively low speeds and low temperature ratios T_w/T_j. They consider the effects of changing impingement plate geometric and configuration parameters, and physical parameters. Spatially-averaged surface heat transfer coefficients beneath an array of impinging jets in low-speed flow for Reynolds numbers from $3x10^2$ to $3x10^4$, *X/D* and *Y/D* from 3.1 to 12.5, and *Z/D* from 1.0 to 4.8 are presented by Kercher and Tabakoff (1970) who employ plate temperatures of 66°C and 107°C with an air temperature of 24°C. Spent air flow from the impingement array is constrained to exit the flow passage in one direction. These investigators report that the spatially-averaged heat transfer coefficients are dominated by the Reynolds number, and streamwise/spanwise hole spacing. Metzger and Korstad (1972) examine the influences of cross-flow on a single line of jets, emerging from circular holes, placed on one wall of a channel, showing that target spacing, jet Reynolds number, and the relative strengths of the jet flow and the cross flow influence heat transfer on the target wall. The jet temperature was the same as the ambient crossflow temperature and the wall temperature of the test block was about 66°C.

Like the investigation of Kercher and Tabakoff (1970), Chance (1974) also investigates low-speed impingement cooling with spent air constrained to flow out only one side of the flow passage. To study the effect of jet temperature, ratios of impingement to surface absolute temperature of 0.77, 1.27, and 1.54 are employed. Jet temperatures between 32°C and 121°C and wall temperatures between 38°C and 121°C are used. This experiment is limited to a comparison between using impingement jets to heat a surface and using impingement for cooling. Heat transfer values for the impinging hot jets are shown to be about 10% greater than values measured for surface cooling experiments. Static pressure variations with the

impingement passage are also described as increasing with higher cross-flow velocities as *Z/d* decreases. Optimal values of *Z/d* are described, which depend upon the ratio of total jet area to heat transfer area, for best heat transfer enhancement. Heat transfer characteristics measured on a target surface beneath a two-dimensional array of impinging jets at low-speed flow is also presented in another paper by Metzger et al. (1979). Investigated are *Z/d* values of 1, 2, and 3, *X/d* and *Y/d* ranging from 6 to 32, and Reynolds numbers from $5x10^3$ to $2x10^4$. The segment surface temperature difference between the maximum power and the zero power is about 15 to 35 *K*. These investigators indicate that in-line jet impingement hole patterns provide better heat transfer than staggered arrangements. A continuation of this investigation is described by Florschuetz et al. (1981), wherein Reynolds numbers from $2.5x10^3$ to $7x10^4$, inline and staggered hole patterns, *Z/d* from 1 to 3, *X/d* from 5 to 15, and *Y/d* from 4 to 8 are considered. In this investigation, the temperature difference between the impingement surface temperature and the plenum air temperature is normally 15 to 30 *K*. As for the previous investigation, impinging air is again constrained to exit in a single direction from the channel formed between the impingement plate and the target plate. Included are data on channel cross flow mass velocity and jet mass velocity (where ratios range from 0 to 0.8), a correlation which gives Nusselt number dependence on these parameters, as well as on jet impingement plate geometry, Prandtl number, and Reynolds number.

Obot and Trabold (1987) consider different cross-flow schemes on impingement heat transfer in low-speed flows. Impingement jet Reynolds numbers from $1x10^3$ to $2.1x10^4$, *Z/d* values from 2 to 16, *X/d* values of 5 and 10, and *Y/d* values of 4 and 8 are employed. Also the average temperature difference of the exiting air with power and without power is 25 to 50 *K*. According to these investigators, for a given crossflow scheme and constant jet diameter *d*, higher heat transfer coefficients are obtained as the number of jets over a fixed target area increases. Bunker and Metzger (1990) present detailed local heat transfer distributions due to line jet impingement for leading edge regions, both with and without film extraction effects. Fox et al. (1993) examine the effects of unsteady vortical structures on the adiabatic

wall temperature distribution produced by a single impinging jet. Secondary vortex structures within the jet are described which alter adiabatic surface temperatures when the target plate is near the jet nozzle (i.e. *Z/d* of 1, 2, or 4). Also important are self-sustaining acoustic resonance events, which, when present, alter adiabatic surface temperature distributions.

In another investigation which employs flat target plates, Brevet et al. (2002) consider one row of impinging jets in a test section with low speed flow in which the spent air is again constrained to exit in one direction. Effects of impingement distance, Reynolds number, and spanwise hole spacing on Nusselt number distributions lead to recommendations for optimal *Z/d* values of 2 to 5, and optimal spanwise hole spacings of 4 to 5 hole diameters. Data obtained at Reynolds numbers from $5x10^3$ to $2x10^4$, *Z/d* of 1, 2, 5, and 10, and *X/d*, *Y/d* values of 2, 4, 6, and 10 also show that local and spatially-averaged Nusselt numbers increase substantially with Reynolds number. For this study, the temperature difference between the wall temperature and the jet temperature is 25ºC to 65ºC. In another study by Brevet et al. (2001), recovery factors and Nusselt numbers measured on a flat target surface beneath a single, compressible impingement jet are described. Results are given for *Z/d* ratios from 2 to 10, at different Mach numbers from 0.02 to 0.69. The wall temperature is about 60º C and the jet total temperature is the same as the ambient temperature. Using different impingement hole plates with different hole diameters from 3 mm to 15 mm, data sets with different Mach numbers and constant Reynolds number are obtained. Park et al. (2007) use a staggered array of holes with spacing of X/D=8, Y/D=8, and Z/D=3. They constrain the spend air cross flow to exit in one direction and report discharge coefficients. They use a variety of impingement hole diameters to vary Mach number independently of Reynolds number to generate a correlation based on that of Florschuetz et al. (1981) which accounts for compressibility effects for jet Reynolds number of 30,000. Goodro et al. (2007) is a continuation of this work that addresses jet Reynolds number of 60,000. Bailey and Bunker (2002) investigate impingement arrays with inline jets in a “square array”, with axial and lateral jet spacings of 3, 6, and 9. Reynolds numbers range from $1.4x10^4$ to $6.5x10^4$, Mach numbers are relatively

low, and jet plate-to-target spacings range from 1.25 to 5.5 impingement hole diameters. Included are correlations developed from these data which extend the range of applicability of the correlations presented by Florschuetz et al. (1981). They also show that, for sparse impingement arrays, each jet behaves independently.

Other recent studies consider the effects of jet impingement on a leading edge/concave wall with roughness (2002), and the effects of jets with mist and steam on a concave target surface (Li et al., 2002). Parsons et al. (2001, 2003), Parsons and Han (2001), Epstein et al. (1985), and Mattern and Hennecke (1996) show that rotational effects are important for jets impinging on flat surfaces at relatively low Reynolds numbers. San et al. (2001) investigate jet-to-jet spacing to optimize surface heat transfer for staggered arrays of impinging air jets. Five jets, two exit sides, and Reynolds numbers between 10,000 and 30,000 are employed. For Reynolds numbers of 10,000-30,000, they recommend optimal jet-to-jet spacings of 8*D*, 12*D*, and 6*D* for jet hole exit to target plate distances of 2*D*, 3*D*, and 5*D,* respectively. Downs et al. (1987), Jambunathan et al. (1992), and Viskanta (1993) present reviews of several other jet impingement investigations.

1.6.2 Film Cooling Literature Survey

Film cooling, as a research topic, has enjoyed widespread attention for many years. As such, there is a wealth of available information in the form of journal and conference publications. Much of this work, like that of Gritsch et al. (2000), is for a single hole. The benefit of this type of work is that the exact effects of the film from a cooling hole can be examined without the interference caused by flow disruptions generated by adjacent holes. Baldauf et al. (2001) use infrared thermography in conjunction with a finite element analysis to determine local heat transfer coefficients of a flat plate downstream a single row of cylindrical holes. They utilize a density ratio of 1.8, film cooling injection angles of 30, 60 and 90, hole spacings of X/D=6 and Y/D=2,3,4, and blowing ratios from 0.2 to 2.5. In a companion paper, the same authors use a similar approach to find local effectiveness values for these conditions (2001). Other authors to examine a single row of film cooling holes include:

Goldstein and Eckert (1974), Yuen and Martinez-Botas (2005), Couthard et al. (2006), Saumweber et al. (2004), and Waye and Bogard (2007). Goldstein and Eckert (1974) study the effects of hole geometry and density on film cooling. They also address the address the effect of using a higher density secondary fluid, concluding that such conditions requires a higher blowing ratio to cause jet separation from the surface resulting in better film cooling. Yuen and Martinez-Botas (2005) study circular holes at inclination angles of 30º, 60º, and 90º with zero pressure gradient and blowing ratios from 0.33 to 2.0. They determined the optimal hole angle and the optimal blowing ratio to be 30º and 0.5 respectively. Couthard et al. (2006) consider blowing ratios of 0.25, 0.5, 1.0 and 1.5 for round holes inclined 35º to the film-cooled surface and provide detailed information on both effectiveness and Stanton number distributions. Saumweber et al. (2004), compare a single row of round holes to a single row of fan shaped holes. It is of note that they use a temperature ratio high enough to generate a density ratio of 1.7 which is comparable to aeroengine combustors. They examine blowing ratios ranging from 0.5 to 2.5 and vary turbulence intensity between 3.6% and 11%. They found that the film from shaped holes remained attached to the surface, even at the increasing blowing ratios that cause the protective film to lift off the cooled surface for the round holes. They also found that increasing turbulence intensity led to decreased sensitivity to blowing ratio for the round holes. Waye and Bogard (2007) examine round compound angle holes which are inclined 45º to the cooled surface and inclined 45º to the flow direction. They use axially aligned, round holes inclined 30º to the cooled surface for comparison. Blowing ratios from 0.2 to 1.4 were examined at density ratios of 1.3 and 1.5 and turbulence intensities of 3.9% and 1.0%. They report higher effectiveness near the holes for blowing ratios of 0.3 and 0.4 compared to the other blowing ratios examined, but are quick to point out the rapid drop in effectiveness with increasing distance from the hole for those cases. The authors report 0.6 as the blowing ratio with the highest overall effectiveness for the round, axially aligned holes. For the compound angle holes they indicate the highest overall effectiveness occurs at blowing ratio 0.4, but that there was little change between a blowing ratio of 0.2 and

0.7, showing less of an effect due to blowing ratio than the axial holes. They conclude the compound angle holes provide better laterally averaged adiabatic effectiveness than the axial holes.

All the film cooling studies for either a single round hole or a row of round holes, which consider blowing ratio, report a sizable decrease in effectiveness for blowing ratios above 0.5. This is because the increased jet momentum with respect to the freestream mass flux generates a phenomenon known as liftoff, where the cooling fluid separates from the film-cooled surface. The protrusion of the jet into the freestream generates vortices which move hot fluid from the freestream directly into contact with the cooled surface beneath the coolant.

In 1979 Sasaki et al. noted that although many film cooling investigations had provided data and correlations for either a single hole, or a row of holes, very little literature was available for an array of film cooling holes. This tendency to study either a single hole or a single row continues today as evidenced by the number of previously mentioned studies published well after 1979. There are however, a number of studies for a full array of film cooling holes which provide valuable data and conclusions. Sasaki et al. (1979) use a staggered array of round holes with a 45º angle of inclination and hole spacing X/D = 10, Y/D = 3. They compare data from this array to a single row of holes for a range of blowing ratios from 0.1 to 1.0. They visually demonstrate the additive nature of successive rows of film cooling holes and find that for blowing ratios from 0.14 to 0.50, the laterally averaged effectiveness generally increases with increasing blowing ratio. Mayle and Camarata (1975) use a full array of compound angle holes, angled 30º with respect to the surface and 45º with respect to the bulk flow direction. They consider spanwise hole spacing Y/D = 8, 10, and 14 with the streamwise spacing equal to 86.6% of the spanwise spacing for each case and blowing ratios 0.5, 1.0, 1.5, and 2.0. They present results in the form of spatially average adiabatic effectiveness with very little variation between a blowing ratio of 1.0 and 2.0. For a blowing ratio of 1.5, the cases for Y/D = 8 and Y/D = 10 are slightly higher, but the Y/D = 14 case remains approximately the same. In all cases, the effect of changing the hole spacing is much more significant than the effect of

varying the blowing ratio. Leger et al. (2002) consider a range of hole angles from 20º to 150º and hole spacings from X/D = 3.5, Y/D = 3.0 to X/D = 2.4, Y/D = 5.8. The density ratio used varies from 2.8 to 4.7. For a 30º hole angle plate, the authors report an increase in effectiveness with increasing blowing ratio, with a 15% change in effectiveness between a blowing ratio of 0.42 and 3.14. Ling et al. (2002) use a staggered array of 20º holes with spacings of X/D = 10, Y/D = 10 and X/D = 16, Y/D = 16. They examine blowing ratios of 0.5, 1.0 and 1.5 with density ratios of ~1.1 and ~1.7. To conclude, they indicate an increase in adiabatic effectiveness at the same blowing ratio for an increase in density ratio and show a sharp drop in effectiveness as blowing ratio increases from 0.5 to 1.5.

While Ling et al. (2002) demonstrate the sharp drop in effectiveness seen for a single row of holes in an array, Lin et al. (2003) show that for a range of blowing ratios from 1 to 4 and hole spacings of X/D = 8, Y/D = 4 and X/D = 5.67, Y/D = 5.67 holes inclined in the direction of the freestream show negligible change with increasing blowing ratio. Furthermore, they indicate blowing ratios in the inclined multihole liner of a gas turbine combustor ranges from 2 to 10. While Leger et al. (2002) report improved effectiveness with increasing blowing ratio, in their test case, a higher blowing ratio also corresponds with higher effectiveness preceding the cooled surface. Additionally, after the first few rows of cooling holes, the changes in effectiveness from one row to the next are approximately equal for each blowing ratio. Scrittore et al. (2007) explain that although there does exist a sizable body of knowledge on multi-hole film cooling most of it does not apply to gas turbine combustors because of the high blowing ratios and dense arrays required. Within their conditions of X/D = 4.9, Y/D = 4.9, blowing ratios 3.2, 3.8, 4.4, and 5.0, and hole angle 30º, they agree with Lin et al. (2003) indicating that Blowing ratio has a negligible effect on full array film cooling. They do however show in increase of 5% in adiabatic effectiveness at the 20th row of film cooling holes for a blowing ratio of 5.0, compared to a blowing ratio of 3.2.

Of the aforementioned papers dealing with full array film cooling, only Sasaki et al. (1979) and Scrittore et al. (2007) address the problem of changing static pressure

along the array. In these cases, this change in static pressure is caused by the increased freestream velocity due to the volumetric addition of coolant after it leaves the film cooling holes. This drop in static pressure along the array leads to increased exit velocity from subsequent rows of holes. This change, along with increasing freestream velocity, causes the blowing ratio to change along the array. Scrittore et al. (2007) report a drop in blowing ratio of roughly 20% from the first row of holes to the 20^{th} row. The flow in a typical axial combustor passes through a film-cooled contraction. This contraction produces a change in static pressure much more significant that that reported by either Sasaki et al. (1979) or Scrittore et al. (2007). The present study is unique and relevant to combustor liner cooling because it addresses the effect of such a contraction at the high blowing ratios and dense film cooling arrays typical for such an application.

Other studies of interest to the present examination on film cooling include those of Oldfield (2008), O'Dowd et al. (2009), Roach (1986), and Gritsch et al. (2001). Oldfield (2008) presents an impulse response processing technique which provides a computationally efficient method for processing transient heat transfer signals. O'Dowd et al. (2009) compare six different approaches for determining spatially-resolved heat transfer coefficients and spatially-resolved adiabatic wall temperatures. They conclude that transient infrared thermography is well suited to obtain detailed, spatially resolved adiabatic wall temperatures. They also conclude that the impulse response method described by Oldfield (2008), while more computationally efficient, gives equivalent results to other transient thermal response measurement techniques with reduced uncertainty and is suitable for use with infrared thermography. Roach (1986) provides design guidelines for the construction of grids intended to generate isotropic turbulence. These guidelines consider pressure losses, turbulence intensity, spectra, correlation functions, and length scales. Gritsch et al. (2001) examine discharge coefficients for axially aligned holes with angles of inclination of 30º, 45º, and 90º and compound angle holes angled 30º with respect to the cooled surface and either 45º or 90º with respect to the bulk flow direction. They

provide correlation curves between pressure ratio and discharge coefficient for each of the cases examined.

1.7 Thesis Organization

Following this introduction, detailed descriptions of the experimental facility, experimental procedure, and experimental results of the impingement study are described in Chapters 2 through 5.

Chapter 2 presents the experimental facility developed by the author, describing its capabilities and assembly. The steps used to determine discharge coefficients, crossflow-to-jet mass flux ratio, local, line-averaged, and area-averaged Nusselt numbers, recovery factor, and spatially averaged adiabatic surface temperature are also explained in Chapter 2. Chapter 3 presents the results and conclusions of the study into the effect of varying temperature ratio on impingement heat transfer. Chapter 4 presents Nusselt number variations with Reynolds number and comparisons of spatially-averaged Nusselt numbers with existing correlations for a range of experimental conditions using incompressible flow only. Chapter 5 is similar to Chapter 4, but the focus is on the deviations from existing correlations with an increasing degree of compressibility. New correlations are also presented, which take Mach number effect into account.

Chapters 6 and 7 provide detailed descriptions of the experimental facility, experimental procedure, and experimental results of the film cooling study. In addition to detailed description of the film cooling facility, chapter 6 outlines the experimental procedures used and the steps taken when reducing raw experimental data into reportable results. Chapter 8 presents the summary and conclusions. It is followed by the appendices.

1.8 The Florschuetz Correlation

The work of L.W. Florschuetz, C.R. Truman, and D.E. Metzger published in 1981 and titled “Streamwise Flow and Heat Transfer Distributions for Jet Array Impingement with Crossflow” examines flow distributions from two-dimensional

arrays of jets impinging normal to a heated surface. As part of their work, they develop and present correlations that predict spanwise averaged, streamwise resolved Nusselt numbers correlated in terms of the individual spanwise row jet Reynolds number, crossflow-to-jet velocity ratio, streamwise hole spacing, spanwise hole spacing, and channel height.

When predicting Nusselt numbers using the correlation of Florschuetz et al. (1981) it is first necessary to find the ratio of crossflow velocity to jet velocity G_c/G_j.

$$\frac{G_c}{G_j} = \frac{1}{\sqrt{2}C_D}\frac{\sinh\beta(x/x_n - 1/2)}{\cosh\beta(x/x_n)} \tag{1.6}$$

where $\beta = C_D\sqrt{2}(\pi/4)/[(y_n/d)(z/d)]$ and $x = x_n(i\text{-}1/2)$, i = 1, 2, 3 . . . The Nusselt numbers are then predicted according to the equation:

$$Nu = A * Re_j^m\,[1 - B[(z/d)(G_c/G_j)]^n]*Pr^{1/3} \tag{1.7}$$

where the coefficients A and B and the exponents m and n each depend on the geometric parameters in Table 1.1 according to the equation: A, m, B, and n = $C(x_n/d)^{n_x}(y_n/d)^{n_y}(z/d)^{n_z}$

Table 1.1. Geometric parameters used in the Florschuetz correlation (1981).

	Inline Pattern				Staggered Pattern			
	C	n_x	n_y	n_z	C	n_x	n_y	n_z
A	1.18	−0.944	−0.642	0.169	1.87	−0.771	−0.999	−0.257
m	0.612	0.059	0.032	−0.022	0.571	0.028	0.092	0.039
B	0.437	−0.095	−0.219	0.275	1.03	−0.243	−0.307	0.059
n	0.092	−0.005	0.599	1.04	0.442	0.098	−0.003	0.304

1.9 List of Publications

1.9.1 Conference Publications and Presentations

Park J., Goodro M., Ligrani P. M., Fox M., Moon H.-K., 2006, "Separate effects of Mach number and Reynolds number on jet array impingement heat transfer," Proceedings of the ASME Turbo Expo, GT2006-90628, pp. 581-597

Goodro M., Park J., Ligrani P.M., Fox M., Moon H.-K., 2007, "Effect of Hole Spacing on Jet Array Impingement Heat Transfer," Proceedings of the ASME Turbo Expo, GT2007-28292, pp. 963-976

Goodro M., Park J., Ligrani P.M., Fox M., Moon H.-K., 2007, "Effect of Temperature Ratio on Jet Array Impingement Heat Transfer," Proceedings of the ASME Turbo Expo, GT2007-28293, pp. 977-989

1.9.2 Archival Journal Publications

Park J., Goodro M., Ligrani P. M., Fox M., Moon H.-K., 2007, "Separate effects of Mach number and Reynolds number on jet array impingement heat transfer," Journal of Turbomachinery, 129 (2), pp. 269-280

Goodro M., Park J., Ligrani P.M., Fox M., Moon H.-K., 2007, "Effects of Mach number and Reynolds number on jet array impingement heat transfer," International Journal of Heat and Mass Transfer, 50 (1-2), pp. 367-380

Goodro M., Park J., Ligrani P.M., Fox M., Moon H.-K., 2008, "Effects of Hole Spacing on Spatially-Resolved Jet Array Impingement Heat Transfer," International Journal of Heat and Mass Transfer, 51 (25-26), pp. 6243-6253

Goodro M., Park J., Ligrani P.M., Fox M., Moon H.-K., 2009, "Effect of Temperature Ratio on Jet Array Impingement Heat Transfer," Journal of Heat Transfer, 131 (1) pp. 012201-1 – 012201-10

Goodro M., Ligrani P.M., Fox M., Moon H.-K., 2009, "The Effects of Mach Number, Reynolds Number and Jet Spacing on Heat Transfer for a Full Array of Impinging Jets," Accepted for publication in the AIAA Journal of Thermophysics and Heat Transfer

Chapter 2

Experimental Facility and Measurement Techniques for the Impingement Study

2.1 Experimental Apparatus

The description of the impingement experimental apparatus is divided into three sections: the impingement flow facility and impingement plate, the target plate test surfaces, and the air pressure and temperature measurements.

2.1.1 Impingement Flow Facility and Impingement Plate

Schematic diagrams of the facility used for heat transfer measurements are presented in Figures 2.1 and 2.2. The facility is constructed of 6.1 mm thick ASTM A38 steel plates, and A53 Grade B ARW steel piping, and is open to the laboratory air at its inlet and exit. Depending upon the required flow conditions, one of two blowers is employed. For the lower Reynolds numbers investigated, a New York Blower Co. 7.5 HP, size 1808 pressure blower is employed. For higher Reynolds numbers, a DRUM Industries, 50 HP, D807 pressure blower is employed. In each case, the air mass flow rate provided to the test section is measured (downstream of whichever blower is employed) using an ASME standard orifice plate, flow-mounted calibrated copper-constantan thermocouples, and Validyne DP15 pressure transducers (with diaphragms rated at 13.8 or 34.5 kPa) connected to DP10D Carrier Demodulators. The blower exits into a series of two plenums arranged in series (the upstream plenum is 0.63 m to a side and the downstream plenum measures 0.63 m x 0.77 m x 0.77 m). A Bonneville cross-flow heat exchanger is located within the plenum which is farther downstream. As the air exits the heat exchanger, and

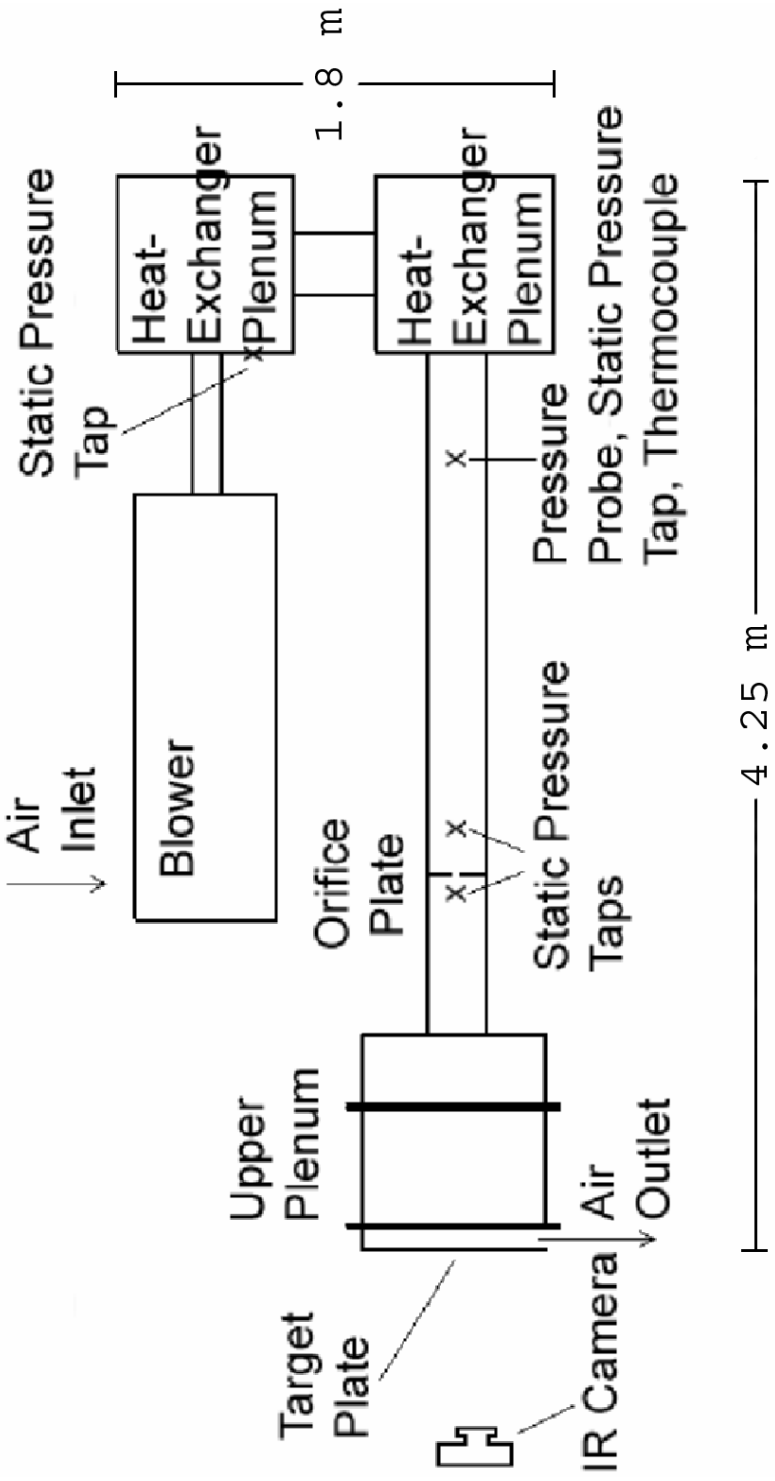


Figure 2.1. Impingement flow facility.

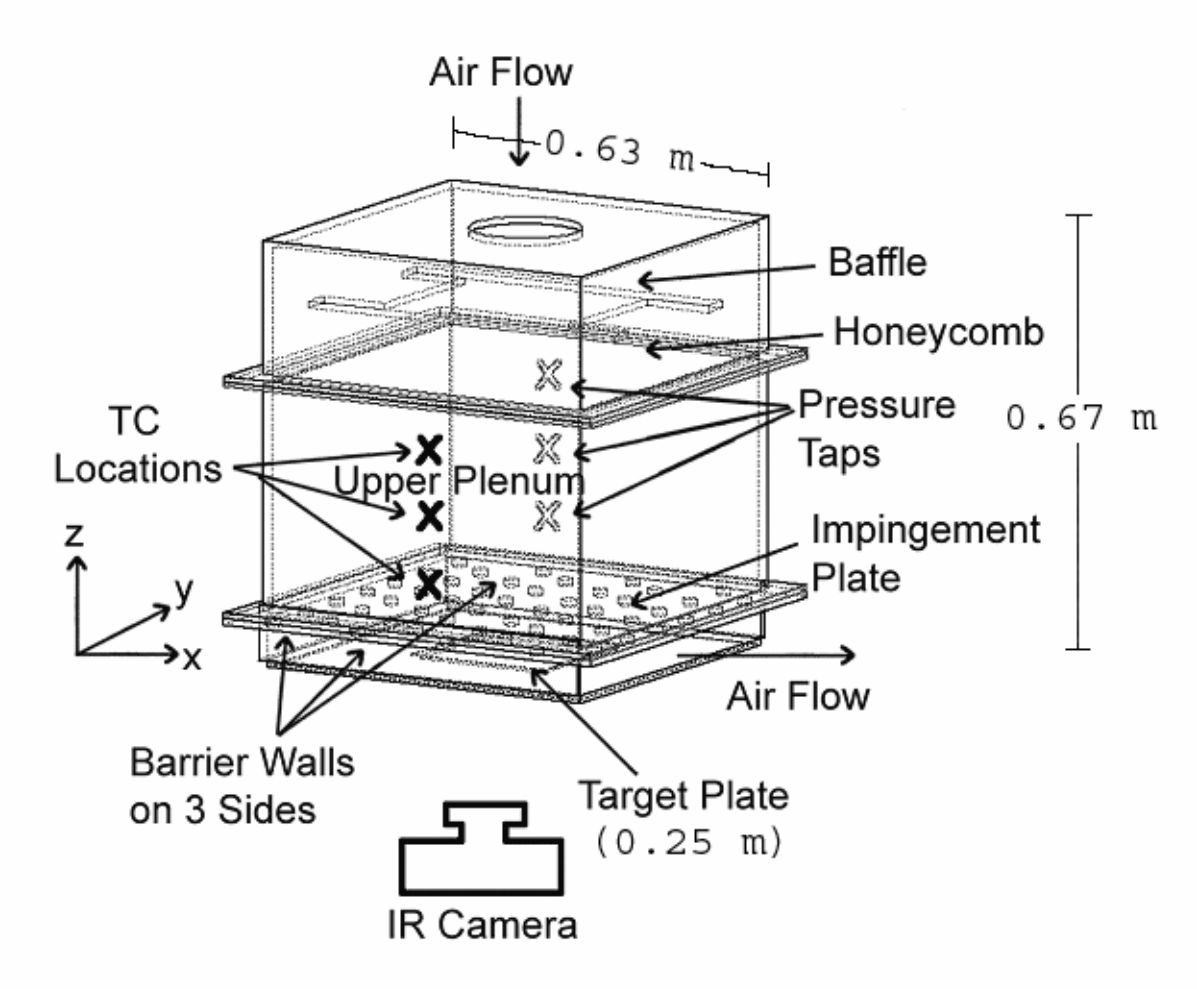


Figure 2.2. Impingement flow facility test section, including impingement plenum, and impingement channel.

the second plenum, the air passes into a 0.22 m outer diameter pipe, which contains the ASME Standard orifice plate employed to measure the air mass flow rate. This pipe then connects to the 0.635 m by 0.635 m side of a plenum. Upon entering this plenum, the air first encounters a flow baffle used to distribute the flow, a honeycomb, and other flow straightening devices. These are followed by the impingement plenum (or upper plenum, located below the honeycomb and flow straightening devices) whose top dimensions are 0.635 m and 0.635 m, and whose height is 0.40 m.

Individual plates with holes used to produce the impingement jets are located at the bottom of this plenum, as shown in Figure 2.2. The plenum is thus designed so that different impingement plates can be installed at this location using a 9.5 mm thick polyurethane gasket and ¼ in SAE J429 Grade 5 bolts. Figure 2.3 shows that each impingement plate is arranged with 10 rows of holes in the streamwise direction, arranged so that holes in adjacent rows are staggered with respect to each other. With this arrangement, either 9 or 10 holes are located in each streamwise row. The spacing between holes in the streamwise direction X is then $5D$, $8D$, or $12D$ and the spanwise spacing between holes in a given streamwise row Y is equal to the spacing in the streamwise direction. The thickness of each impingement plate is $1D$. The spacing between the hole exit planes and the target plate is denoted Z and is equal to $3D$. Note that the coordinate system employed is also shown in Fig. 2.3. The impingement cooling flow which issues from these holes is contained within the channel formed by the impingement jet plate and the target surface, and is constrained to exit in a single direction, which here, is denoted as the x-direction. This channel is called the lower

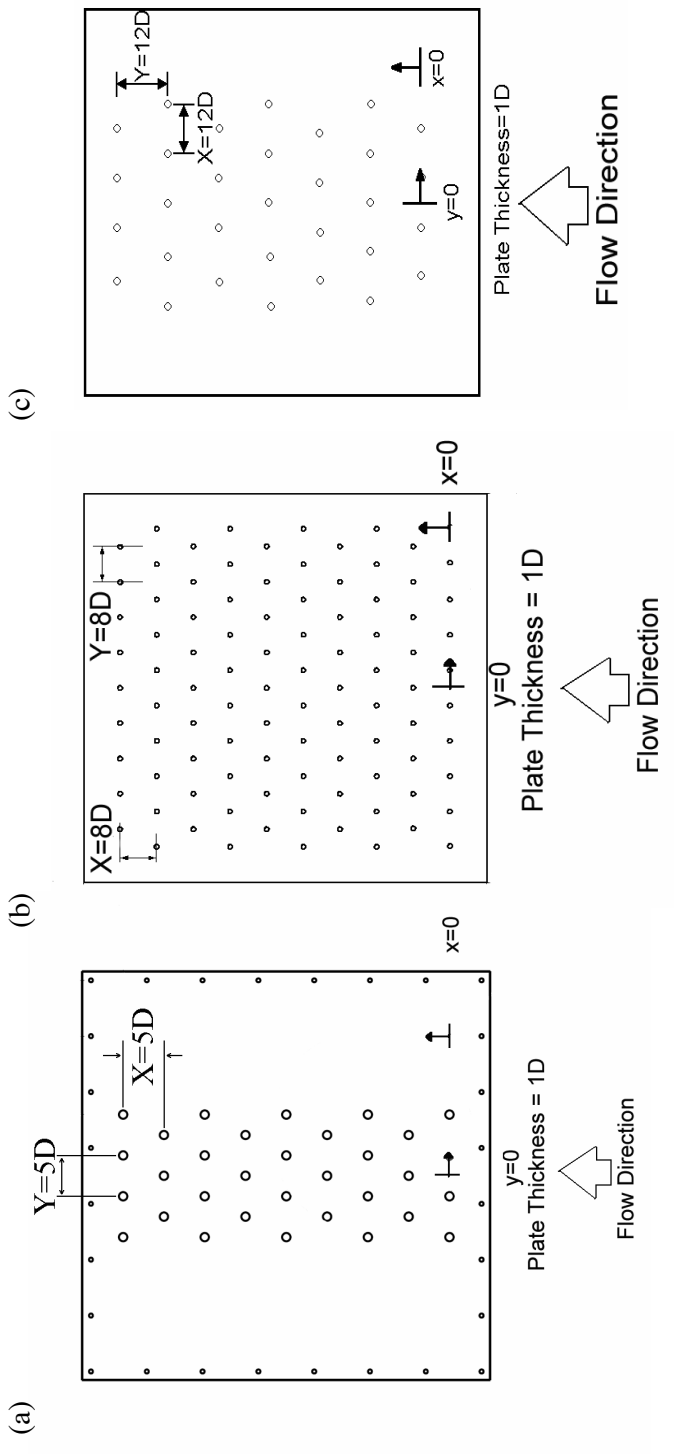


Figure 2.3. Impingement test plate configurations. (a) $X/D=Y/D=5$. (b) $X/D=Y/D=8$. (c) $X/D=Y/D=12$.

plenum. As different plates are employed with different sized impingement holes, this is accomplished using different polycarbonate spacers which are exactly $3D$ in height, and are sealed in place around three sides of the impingement channel. Plates with different impingement hole diameters are used to provide data at a variety of Mach numbers and Reynolds numbers. Specific hole sizes, mass flow rates, and pressure levels are employed so that data are obtained at different Mach numbers as the Reynolds number is constant, and at different Reynolds numbers as the Mach number is constant.

When the effects of T_w/T_j temperature ratio are considered, the impingement air is circulated in a closed loop, so that this air can be cooled to temperatures as low as -80°C. This cooling is implemented using liquid nitrogen in the Bonneville heat exchanger. In order to avoid formation of frost from moisture contained in the air which passes and circulates in the facility, it is first cooled to a temperature of approximately 0°C for a period of at least one hour to allow condensation of as much water vapor as possible. As the facility is cooled to even lower temperatures, this liquefied water then freezes at locations which do not inhibit the passage of the impingement air throughout the facility heat exchangers and other vital areas.

2.1.2 Target Plate Test Surfaces

Two different types of target plates are employed. Polycarbonate target plates are used for measurement of spatially-resolved distributions of surface adiabatic surface temperature and surface recovery factor. Polycarbonate is chosen because of its strength, its low thermal conductivity (0.16 W/mK at 20°C), and to minimize streamwise and spanwise conduction along the test surface, and thus, minimize "smearing" of spatially varying temperature gradients along the test surface. Each plate is 1.58 mm thick, and is mounted on the bottom surface of the plenum using

grey cloth tape with PVC cement, a solvent containing methyl ethyl ketone, tetrahydrofuran, and acetone to seal the edges so that no leaks are present along the flow passage. A mounting frame is also employed to hold the target plate in place, to keep it smooth (without bending or wrinkles), and normal to the impingement jets, as testing is underway. Ten calibrated, copper-constantan thermocouples are placed at different streamwise and spanwise locations within the polycarbonate so that each senses a different temperature as data are acquired. Each one of these thermocouples is mounted approximately 0.016 cm just below the surface adjacent to the air containing the impingement fluid, to provide measurements of local surface temperatures, after correction for thermal contact resistance and temperature drop through the 0.016 cm thickness of polycarbonate. Thermocouple lead wires are placed in grooves along the polycarbonate, and bonded into place with epoxy, to minimize thermal disturbances resulting from their presence.

Spatially-resolved distributions of surface heat transfer coefficients and Nusselt numbers are measured on polystyrene target plates with heaters and thermocouples attached. The custom-made HK5184R26 thermofoil heaters employed are manufactured by Minco Products Inc., and have a temperature rating of 100°C. The etched-foil heating element within this device is encased between two layers of DuPont Kapton polyimide film, and is used to provide a constant surface heat flux boundary condition. This heater is located adjacent to the air stream with the impinging air jets. Its thermal conductivity is 0.2 W/mK at 20°C. Polystyrene is chosen for the target plate because of its strength, and because it does not deform in shape at temperatures as high as 80°C. It is also suitable because of its low thermal conductivity (0.09 W/mK at 20°C), which results in minimal streamwise and spanwise conduction along the test surface. The back side of this polystyrene plate is

viewed by the infrared camera as spatially-resolved measurements of surface temperature are obtained. Each polystyrene target plate is 1.27 mm thick and each heater is approximately 0.3 mm thick, giving a total target plate thickness of 1.57 mm. Like the recovery factor target test plates, and these plates are mounted on the bottom surface of the plenum using grey cloth tape with PVC cement to seal the edges so that no leaks are present along the flow passage. A mounting frame is also again employed to hold the target plate in place, to keep it smooth (without bending or wrinkles), and normal to the impingement jets, as testing is underway. In order to detect different surface temperatures as testing is underway, nine calibrated, copper-constantan thermocouples are placed at different streamwise and spanwise locations within the polystyrene. Each one of these is mounted just below the surface adjacent to the air containing the impingement fluid, between the thermofoil heater and the polystyrene portion of the target plate. As each thermocouple is used to measure local surface temperature, corrections are made for thermal contact resistance and local temperature drop through the thermofoil heater. Thermocouple lead wires are placed in grooves in the polystyrene, and bonded into place with epoxy, to minimize thermal disturbances resulting from their presence. Because of the wear and degradation which results from exposure to different temperature levels as tests are conducted, these target plates are replaced with all new components after about 3 or 4 individual test sequences.

2.1.3 Local Impingement Air Pressure and Temperature Measurements

As shown in Fig. 2.2, three wall pressure taps are located on the surface of the upper plenum. Eight wall pressure taps are also located on the surface of the lower plenum for measurement of local static pressures. As tests are conducted, Validyne Model DP15-46 pressure transducers (with diaphragms rated at 13.8 or 34.5 kPa)

driven by DP10D Carrier Demodulators are used to sense pressures from these static pressure tappings. Local airflow recovery temperatures are measured using two calibrated copper-constantan thermocouples located in the central part of the lower plenum, and three calibrated copper-constantan thermocouples located in the central part of the upper plenum. In each case, readings from either multiple thermocouples or multiple pressure taps are used to obtain average values of measured quantities for a given plenum. In some cases, additional surface pressure taps are located on exit side of the plate with the impingement holes. Voltages from the carrier demodulators and all thermocouples employed in the study are read sequentially using Hewlett-Packard HP44222T and HP44222A relay multiplexer card assemblies, installed in a Hewlett-Packard HP3497A low-speed Data Acquisition/ Control Unit. This system provides thermocouple compensation electronically such that voltages for type T copper-constantan thermocouples are given relative to 0^{o}C. The voltage outputs from this unit are acquired by the Dell Precision 530 PC workstation through its USB port, using LABVIEW 7.0 software and a GPIB-USB-B adaptor made by National Instruments. All data acquisition is controlled using National Istruments LabVIEW using code developed by the author with contributions from Dr. Jongmung Park. Discharge coefficients and crossflow ratios were determined using code originally written in FORTRAN by Dr. Park and later ported to Matlab by the author. Nusselt numbers were determined and organized into usable form using Matlab code developed by Dr. Park and later modified by the author.

Because the overall volume and cross-sectional area of the upper plenum are large compared to the area of the impingement holes, the velocity and Mach number of the air in this plenum are both near zero. As a result, the static pressure measured at the wall static pressure taps is the same as the stagnation pressure, and is denoted P_{oj} ,

the impingement air stagnation pressure. The measured air recovery temperature in the upper plenum is then the same as the upper plenum static temperature and upper plenum stagnation temperature. This resulting value is denote T_{oj}, the impingement stagnation temperature. After measurement of the impingement air mass flow rate at the pipe orifice plate, the impingement air mass flux is determined using $\rho_a u_a = \dot{m} / A$.

An iterative procedure is then used to determine the impingement static temperature T_j, and the impingement flow Mach number M_a. The first step in this procedure is estimation of the value of T_j. The local recovery temperature, which is measured in the lower plenum, is used for this estimation. The impingement static density, and spatially-averaged impingement jet velocity are then determined using $\rho_a = P_a / RT_j$, and $u_a = \dot{m} / \rho_a A$, respectively. Because the impingement flow vents to the laboratory, the local atmospheric pressure is used for P_a. Measurements of lower plenum static pressures using wall pressure taps confirm this approach. Next, the impingement air sonic velocity and Mach number are given by $c_a = (kRT_j)^{1/2}$ and $M_a = u_a / c_a$, respectively. Iterations using these analysis steps are then continued until the impingement static temperature and impingement Mach number are consistent with the isentropic equation given by

$$T_j = T_{oj} / [1 + M_a^2 (k-1)/2] \qquad (2.1)$$

With impingement static temperature T_j, impingement flow Mach number M_a, and other parameters known, the impingement Reynolds number is subsequently given by an equation of the form

$$\mathrm{Re}_j = \rho_a u_a D / \mu_a \qquad (2.2)$$

A Kiel-type stagnation pressure probe is used to measure the total pressure in the pipe at a position which is located upstream of the orifice plate employed to measure mass flow rate. A wall pressure tap located on the surface of the pipe, and a calibrated copper-constantan thermocouple positioned within the air stream are used to sense static pressure and flow recovery temperature, respectively, at the same streamwise location. Pressures and temperatures measured using the thermocouple, probe, and tap are sensed and processed using the same types of instrumentation mentioned earlier. The velocities deduced from this arrangement are used to provide a cross-check on the velocities deduced from mass flow rates, which are measured using the ASME standard orifice plate.

2.2 Experimental Procedure

A wide range of information is obtained when running an impingement experiment and processing the obtained data. This information includes: discharge coefficients, local recovery factors, local Nusselt numbers, and spatially-averaged adiabatic surface temperatures. Experimental uncertainty estimates and baseline Nusselt numbers are also presented.

2.2.1 Discharge Coefficient Determination

The discharge coefficient is determined using

$$C_D = \rho_a u_a / \rho_i u_i \tag{2.3}$$

The first step in determining the ideal impingement mass flux $\rho_i u_i$ is obtaining an ideal impingement Mach number M_i using

$$P_{oj} / P_a = [1 + M_i^2 (k-1)/2]^{k/k-1} \tag{2.4}$$

Next, impingement ideal static temperature T_i is determined using T_{oj}, the ideal Mach number M_i, and the appropriate ideal gas isentropic relationship. Impingement

ideal static density is given by $\rho_i = P_a / RT_i$, and impingement ideal velocity is given by $u_i = M_i(kRT_i)^{1/2}$. Note that, in most cases, discharge coefficients are determined which are based on P_a, the spatially-averaged static pressure at the exits of the impingement holes. In some other cases, local discharge coefficients for different impingement holes located along the length of the plate are determined, which are based on measurements of local static pressure measured at different surface pressure taps located along the exit side of the impingement plate.

2.2.2 Local Recovery Factor Measurement

After the static temperature and stagnation temperatures of the impingement air are determined, the local surface recovery factor is determined at different target surface locations using

$$RF = (T_{aw} - T_j)/(T_{oj} - T_j) \qquad (2.5)$$

Here, T_{aw} represents the local adiabatic surface temperature which is present with zero heat flux on the target surface. Note that some small variations of local adiabatic surface temperature T_{AW} and local recovery factor RF are present due to streamwise and spanwise conduction along the test surface, but these are minimized by the use of the polycarbonate target plate, and are included in the estimates of experimental uncertainty values for these two quantities. As tests are conducted and data are acquired, the impingement air jet stagnation temperature is maintained at or very near to the laboratory ambient temperature level $T_{oj}=T_{ambient}$. This is accomplished using liquid nitrogen in the Bonneville heat exchanger to cool the impingement air to the appropriate level as it passes through the facility. This thermal condition, $T_{oj}=T_{ambient}$, is then maintained for both the Nusselt number experiments and the recovery factor experiments to provide an appropriate basis of comparison between the data obtained from these two different types of experiments.

2.2.3 Local Nusselt Number Measurement

The power to the thermofoil heater, mounted on the target plate, is controlled and regulated using a Variac power supply. Energy balances, and analysis to determine temperature values on the two surfaces of the target plate, then allow determination of the magnitude of the total convective power (due to impingement cooling) for a particular test. To determine the surface heat flux (used to calculate heat transfer coefficients and local Nusselt numbers), the total convective power level, provided by the particular thermofoil heater employed, is divided by the single surface area of this heater, denoted A_{ht}.

One step in this procedure utilizes a one-dimensional conduction analysis, which is applied between the surface *within* the target plate where the thermocouples are located (between the heater and the polystyrene target plate), and the ambient air environment behind the target plate. This is used to determine T_b, the local temperature on the back surface of the polystyrene target plate, adjacent to the surrounding ambient air environment. Also required for this analysis is T_{tc}, the local temperature within the target plate between the heater and the polystyrene plate, which is determined from thermocouple measurements. With these temperatures known, the radiation heat flux and the convection heat flux from the back side of the target plate, q_{rb} and q_{cb}, respectively, are determined together using an equation of the form

$$q_{rb} + q_{cb} = h_{loss}(T_b - T_{ambient}) \qquad (2.6)$$

where h_{loss} is assumed to be equal to 15 W/m^2K (Bailey & Bunker, 2002). The radiation heat flux q_{rf} on the front (or impingement side) of the target plate is determined using

$$q_{rf} = \sigma(1/\varepsilon_{\inf} - 1/\varepsilon_f - 1)^{-1}(T_w^4 - T_{ambient}^4) \quad (2.7)$$

With this approach, the radiation heat flux is determined for an arrangement with multi-reflection between two infinite plates where each has a uniform temperature. ε_f and $\varepsilon_{\inf}$ are assumed to be equal to 0.9 for all conditions investigated. This approximate approach works well since $q_{rf}A_{ht}$ is generally only 3-6 percent of Q, the total amount of power provided to the thermofoil heater. Note that T_w, the local target surface temperature on the surface of the heater adjacent impingement air, must be known to determine q_{rf}. Because of the inter-dependence of T_w, q_{rf}, and q_{cf} (the convection heat flux from the front side or impingement side of the target plate), an iterative procedure is required to determine these quantities. The next part of this procedure uses a one-dimensional conduction model for the heater, which includes source generation of thermal energy, to provide a relation between T_W, T_{tc}, and q_{cf}. Also included in the analysis is thermal contact resistance between the internal thermocouples and the adjacent heater.

The convection heat flux from the front side (or impingement side) of the target plate is then given by

$$q_{cf} = Q/A_{ht} - q_{rf} - q_{rb} - q_{cb} \quad (2.8)$$

The local Nusselt number is then given as

$$Nu = q_{cf}D/((T_w - T_{oj})\alpha) \quad (2.9)$$

Modified local Nusselt numbers are also determined, which are based on the $(T_w - T_{oj}^*)$ and the $(T_w - T_{aw})$ temperature differences. The determination of these parameters is discussed in section 2.2.4. Figure 2.4 provides a representation of the target plate cross section to aid in the visualization of the heat fluxes and temperatures involved.

Spatially-resolved temperature distributions along the target test surface are determined using infrared imaging in conjunction with thermocouples, energy balances, digital image processing, and *in situ* calibration procedures. These are then used to determine spatially-resolved surface Nusselt numbers. To accomplish this, the infrared radiation emitted by the heated interior surface of the channel is captured using a Thermacam PM390 Infrared Imaging Camera, which operates at infrared wavelengths from 3.4 μm to 5.0 μm, or alternatively, using a FLIR Systems Inc. ThermoVision® A20M Compact Temerature Measurement IR Camera (S/N 22700776), which operates at infrared wavelengths from 7.5 μm to 13.0 μm. Temperatures, measured using the calibrated, copper-constantan thermocouples distributed along the test surface adjacent to the flow, are used to perform the *in situ* calibrations simultaneously as the radiation contours from surface temperature variations are recorded.

This is accomplished as the camera views the test surface from behind, as shown in Fig. 2.2. In general, six thermocouple junction locations are present in the infrared field viewed by the camera. The exact spatial locations and pixel locations of these thermocouple junctions and the coordinates of the field of view are known from calibration maps obtained prior to measurements. During this procedure, the camera is focused, and rigidly mounted and oriented relative to the test surface in the same way as when radiation contours are recorded. Voltages from the thermocouples are acquired using the apparatus mentioned earlier. With these data, gray scale values at pixel locations within digital images from the infrared imaging camera are readily converted to local Nusselt number values. Because such calibration data depend

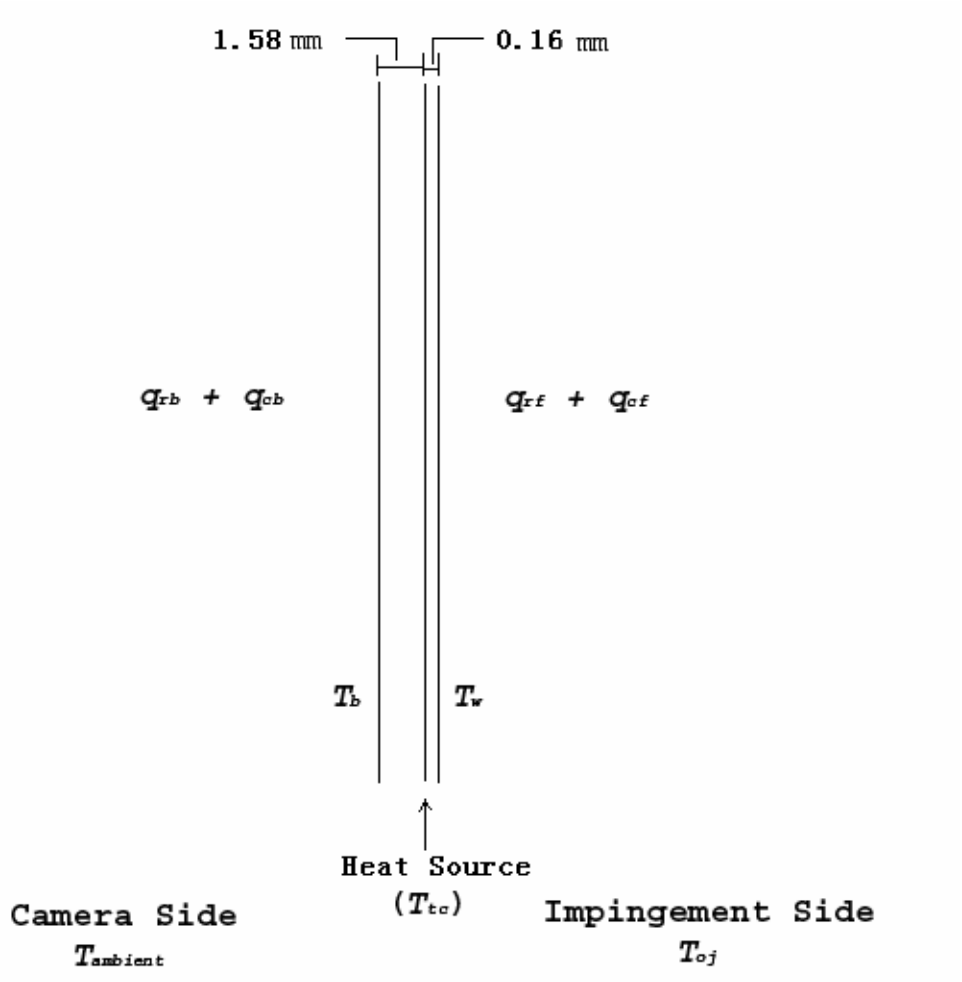


Figure 2.4.Target plate cross section.

strongly on camera adjustment, the same brightness, contrast, and aperture camera settings are used to obtain the experimental data. The *in situ* calibration approach rigorously and accurately accounts for these variations.

Images from the infrared camera are recorded as 8-bit grey scale directly into the memory of a Dell Dimension XPS T800r PC computer using a Scion Image Corporation Frame grabber video card, and Scion image v.1.9.2 software. One set of 15 to 20 frames is recorded at a rate of about one frame per second. All of the resulting images are then ensemble averaged to obtain the final gray scale data image. This final data set is then imported into Matlab version 6.1.0.450 (Release 12.1) software to convert each of 256 possible gray scale values to local Nusselt number at each pixel location using calibration data. Each individual image covers a 256 pixel by 256 pixel area.

2.2.4 Determination of Spatially-Averaged Adiabatic Surface Temperature T_{oj}^*

To determine an appropriate reference temperature to determine heat transfer coefficients and Nusselt numbers, the convective heat power from front side (or impingement side) of the target plate q_{cf} is plotted as it varies with $(T_w - T_{oj})$. An example of such a plot for Re_j = 30,500 and M_a =0.2 is shown in Fig. 2.4. Here, data are obtained at three different temperature differences. The largest temperature difference employed is always less than 30°C to avoid variations of measured Nusselt numbers with variable property effects. As a result, convective heat power data like that presented in Fig. 2.5 vary linearly with $(T_w - T_{oj})$. Such linear data are extrapolated to the q_{cf} =0 axis to determine $(T_w - T_{oj}^*)$. Note that the convective power is the value for the entire target plate. Consequently, the magnitude of T_{oj} * is spatially-averaged over the target plate heat transfer area, and as such, is the

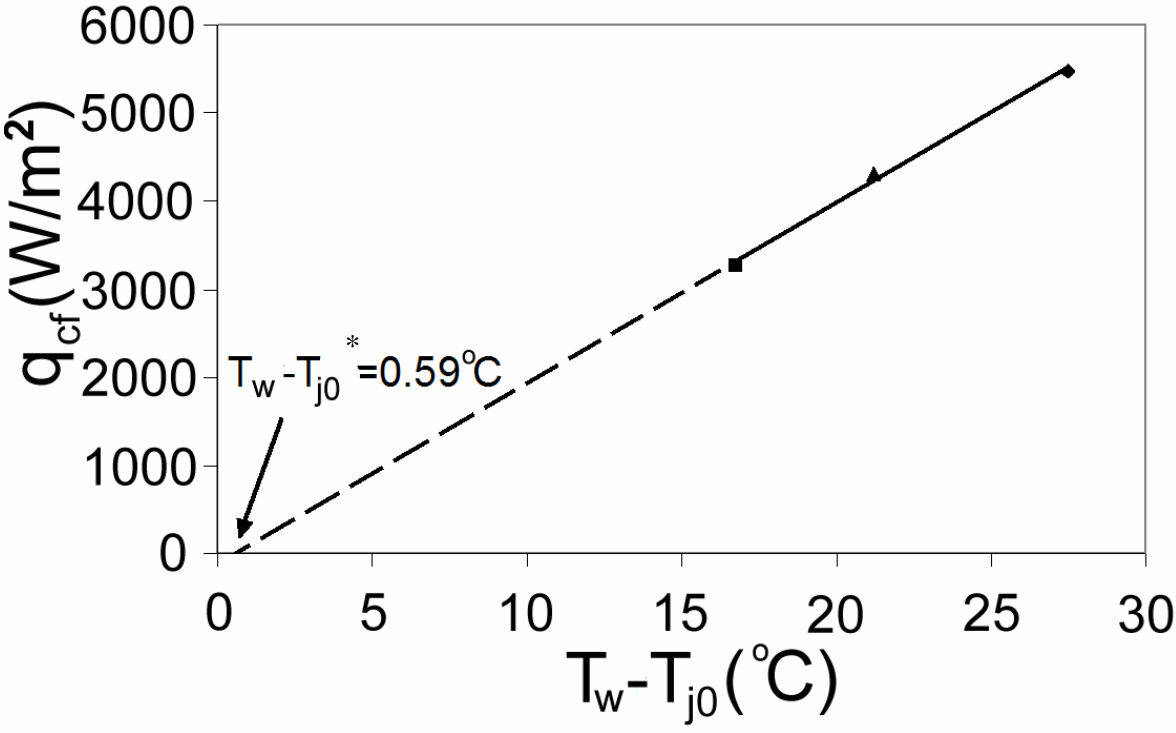


Figure 2.5. Convection heat power from front side (or impingement side) of the target plate q_{cf} as it varies with $(T_w - T_{oj})$ for $Re_j = 30{,}500$ and $Ma = 0.2$ for hole spacing $X/D, Y/D = 8$.

spatially-averaged adiabatic surface temperature for the entire heated portion of the target plate at a particular experimental condition. Consequently, all Nusselt number data are obtained at three different values of $(T_w - T_{oj})$ to provide a means to determine T_{oj}* for each experimental condition. All Nusselt numbers are then calculated using

$$Nu = q_{cf} D / (A_{ht} (T_w - T_{oj}^*) \alpha) \qquad (2.10)$$

2.2.5 Experimental Uncertainty Estimates

Uncertainty estimates are based on 95 percent confidence levels and are determined using methods described by Kline and McClintock (1953) and Moffat (1988). Uncertainty of temperatures measured with thermocouples is ±0.15°C. Spatial and temperature resolutions achieved with infrared imaging are about 0.1 mm to 0.2 mm, and 0.4°C, respectively. This magnitude of temperature resolution is due to uncertainty in determining the exact locations of thermocouples with respect to pixel values used for the *in situ* calibrations. Local Nusselt number uncertainty is then about ±4.8 percent. Uncertainty magnitudes of local recovery factors and adiabatic surface temperatures are approximately ±2.4 percent, and 0.5°C, respectively. Note that uncertainties of local Nusselt numbers, adiabatic surface temperatures, and recovery factors all include the effects of very small amounts of streamwise and spanwise conduction along the test surfaces employed. Reynolds number uncertainty is about ±2.0 percent for an Re_j value of 20,000.

2.2.6 Baseline Nusselt Numbers

Baseline Nusselt numbers are measured using a test plate and flow conditions which match ones used by Florschuetz et al. (1981) with Re_j = 34,500, Ma approximately equal to 0, and an array of jets with $X = 5D$, $Y = 4D$, and $Z = 3D$. In both cases, the effects of spent air cross-flow are considered, and the passage between

the impingement plate and the target plate is closed on 3 sides. Figure 2.6 shows a comparison of results from the two investigations. The present data, line-averaged over Y/D from -8.0 to +8.0, and area-averaged also over Y/D from -8.0 to +8.0 and over $5D$ length segments in the streamwise direction, are compared to area-averaged data from Florschuetz et al. (1981) in Fig. 2.6. The good agreement of the area-averaged data from the two sources validates the experimental procedures and apparatus employed in the present study. Also presented in this plot are local Nu data from the present investigation for $Y/D = 4$ and $Y/D = 8$.

Also investigated is the effect of the unheated starting length located upstream of the heated target plate. This is important because only the target plate is heated and in many cases it represents only a small percentage of the area under impingement jets as is the case for the configurations presented in figs. 2.2 and D.5. The effect is determined by adding an extra heater upstream of the heater used on the target plate. Local and spatially-averaged Nusselt numbers are then measured on the target plate, both with and without upstream heating, for Re_j = 34,500 and M_a = 0.12 with the same impingement hole plate as used for the other baseline data checks. The variation of local and spatially-averaged Nusselt numbers between the two tests is only about two percent, at most, indicating minimal effect of thermal entry length on impingement heat transfer (for these particular experimental conditions).

2.2.7 Impingement Flow Characteristics

Gauntner et al. (1970) describe the types of flow associated with a single impinging jet. They characterize four distinct flow regions and provide a figure to aid in visualization (Fig. 2.7). Region I extends from the exit of the impingement hole to

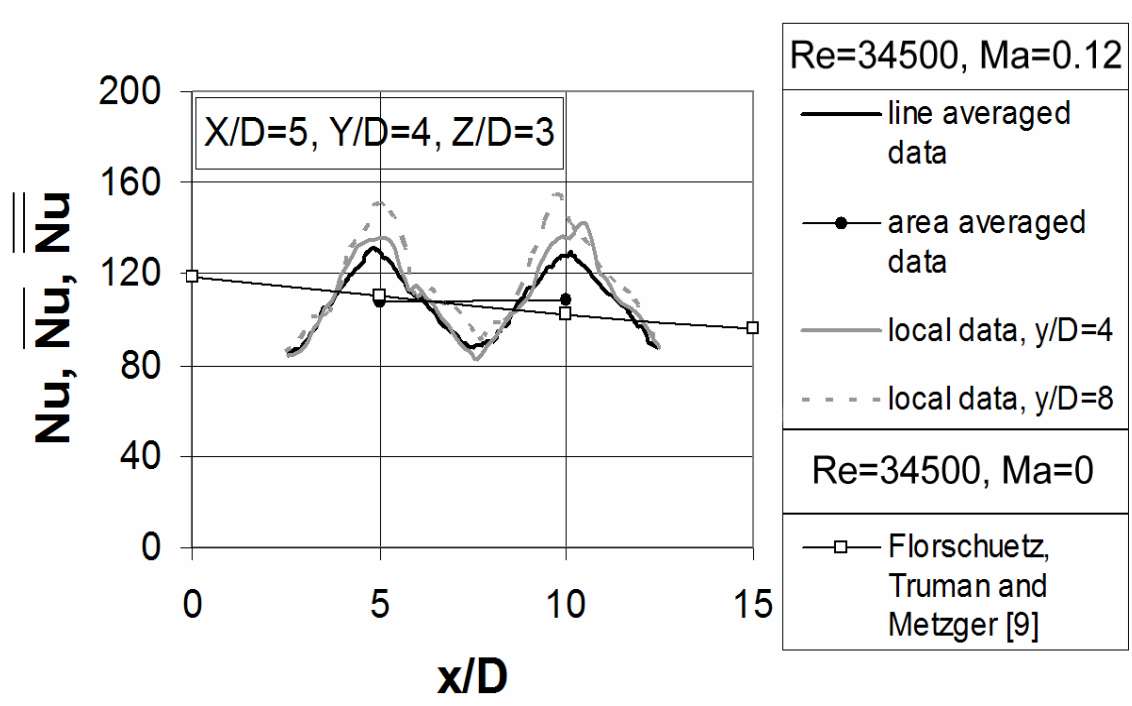


Figure 2.6. Comparison of baseline Nusselt number data with correlation of Florschuetz et al. (1981) for $Re_j = 34{,}500$, Ma approximately equal to 0, and an array of jets with $X = 5D$, $Y = 4D$, and $Z = 3D$.

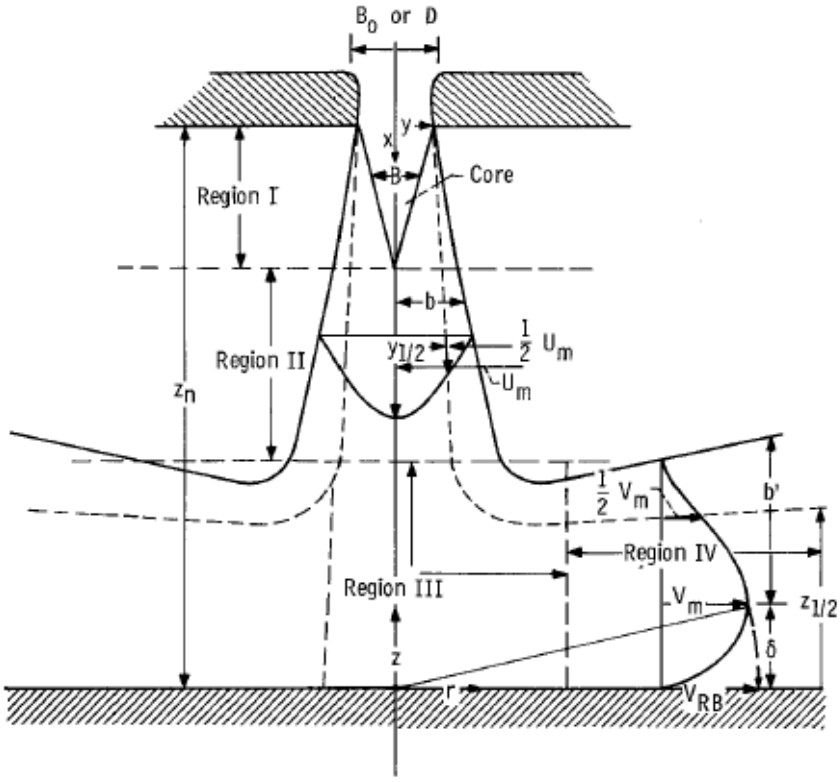


Figure 2.7. Characteristic regions in impinging jet flow as presented in Gauntner et al. (1970).

the end of the potential core, where the potential core is understood to be the central portion of the flow with velocity equal to the velocity at the exit of the impingement hole. The primary characteristics of region II are the dissipation of centreline jet velocity and the lateral expansion of the jet. Region III is the region where deflection of the jet from the axial direction occurs. The wall jet region (region IV) is characterized by increasing thickness of the deflected flow as the boundary layer develops.

Chapter 3

Effect of Temperature Ratio on Jet Array Impingement Heat Transfer

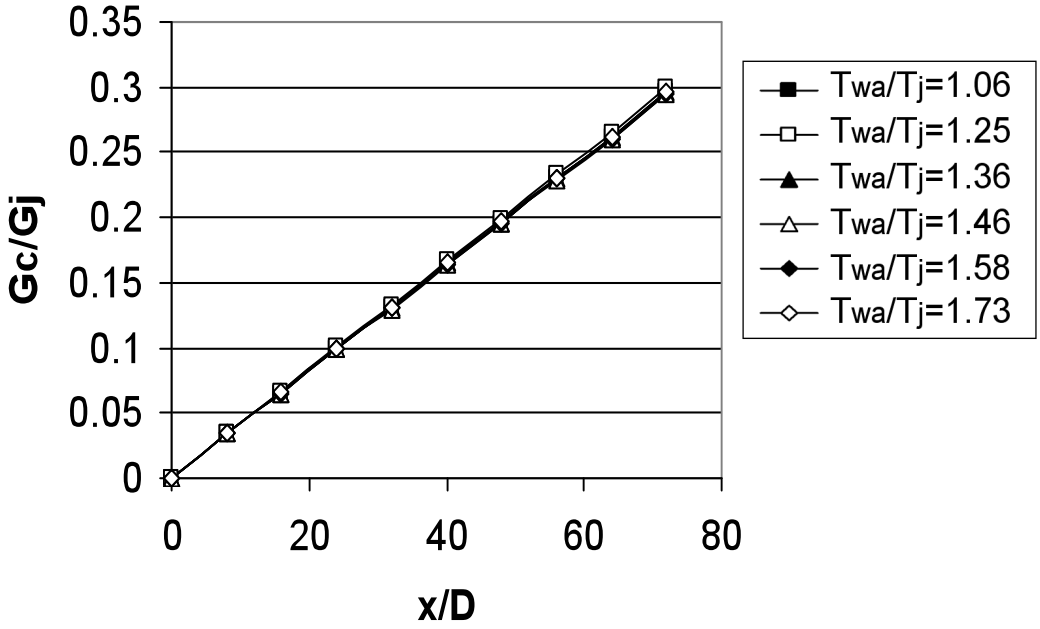
3.1 Overview

Considered are the effects of temperature ratio on the heat transfer from an array of jets impinging on a flat plate. At constant Reynolds number of 18000, and constant Mach number of 0.2, different ratios of target plate temperature to jet temperature are employed. The spacing between holes in the streamwise direction X is 8D, and the spanwise spacing between holes in a given streamwise row Y is also 8D. The target plate is located 3D away from the impingement hole exits. Experimental results show that local, line-averaged, and spatially-averaged Nusselt numbers decrease as the T_{wa}/T_j temperature ratio increases. This is believed to be due to the effects of temperature-dependent fluid properties, as they affect local and global turbulent transport in the flow field created by the array of impinging jets. The effect of temperature ratio on crossflow-to-jet mass velocity ratio and discharge coefficients is also examined.

3.2 Crossflow-to-Jet Mass Flux Ratio and Discharge Coefficients

In many situations, an increase in the mass velocity of the crossflow G_c decreases the effectiveness of the impingement jets, therefore a high value of the crossflow-to-jet mass velocity ratio G_c/G_j is undesirable. As the intensity of the crossflow increases, the momentum of each individual jet is increasingly diverted in the direction of the crossflow. Fig. 3.1a shows the distribution of this quantity as it varies in the streamwise direction determined by adding the mass flow from each

(a)



(b)

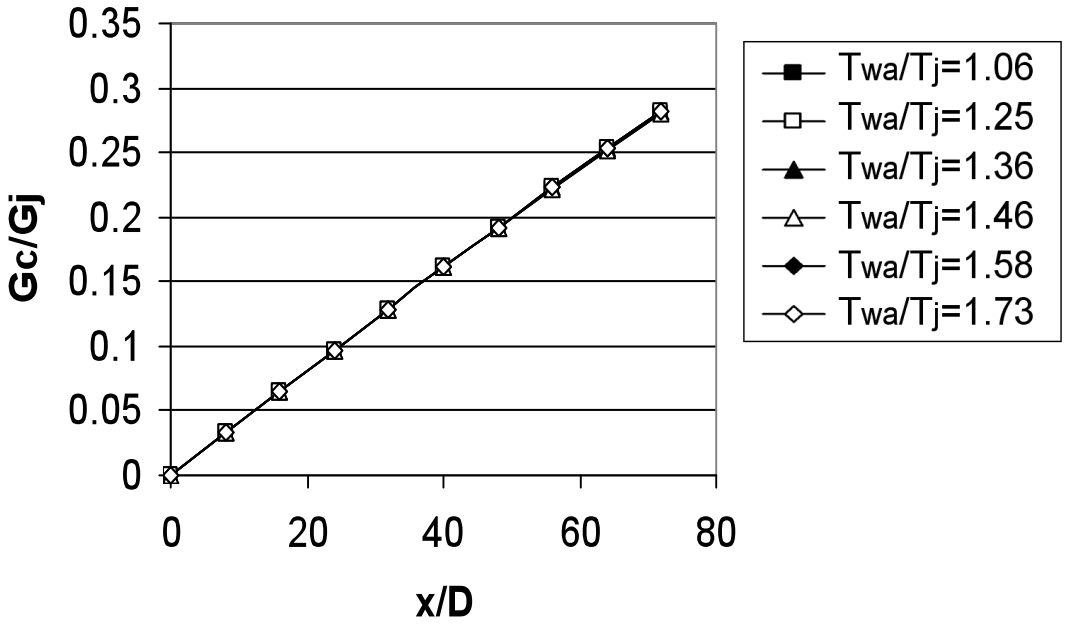


Figure 3.1. (a) crossflow-to-jet mass velocity ratio distribution in streamwise direction determined experimentally (b) crossflow-to-jet mass velocity ratio distribution in streamwise direction predicted using the Florscheutz et al. (1981) correlation

subsequent row of holes. The mass flux for each individual hole is found by dividing the total mass flux as measured by the orifice plate by the number of holes. This is a valid approach because the change in static pressure along the impingement plate is less than 0.1% of the driving pressure difference. Fig. 3.1b presents G_c/G_j values determined using the correlation of Florschuetz et al. (1981). G_c/G_j values from the two methods show good agreement with each other at each value of x/D and T_w/T_j. Note that G_c/G_j variations with x/D are approximately the same regardless of the value of T_{wa}/T_j. In both cases, the ratio of the crossflow-to-jet mass velocity is close to linear and is below 0.3 at the furthest downstream row. Fig. 3.2 shows that the discharge coefficient remains approximately constant as the temperature ratio changes.

3.3 Local Surface Nusselt Number and Line-Averaged Nusselt Number Variations With Temperature Ratio.

Figures 3.3-3.8 show the effects of T_{wa}/T_j temperature ratio on local, line-averaged, and spatially-averaged Nusselt number data for Re_j = 18,000 and Ma = 0.2. These data at different increasing values of T_{wa}/T_j are obtained by decreasing the impingement jet static temperature T_j and increasing T_{wa}, where T_{wa} is the spatially-averaged target wall temperature, and T_j is the impingement jet static temperature.

Surface Nusselt number distributions are presented in Fig. 3.3 for Ma = 0.20, Re_j = 18,000, and T_{wa}/T_j = 1.06, 1.25, 1.36, 1.48, 1.58, and 1.73. Note that, regardless of the temperature ratio, the qualitative distributions of local Nusselt number produced by each impingement jet are similar, with good periodic repeatability in the spanwise direction for each streamwise row of impact locations. Figure 3.3 also shows that each impingement jet produces only one local maximum value in the Nu

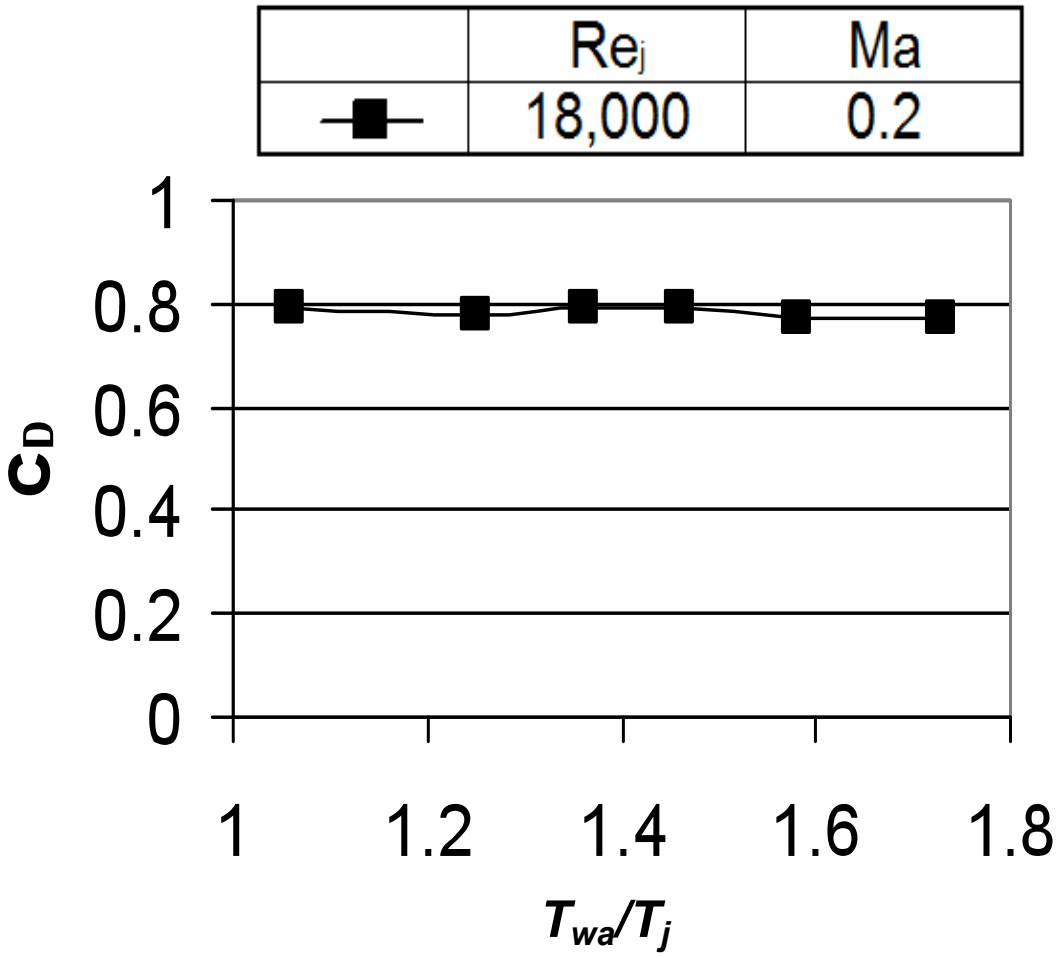


Figure 3.2 Discharge coefficient in streanmwise direction for Re_j = 18100, Ma = 0.2, and T_{wa}/T_j = 1.06, 1.25, 1.36, 1.46, 1.58, 1.73.

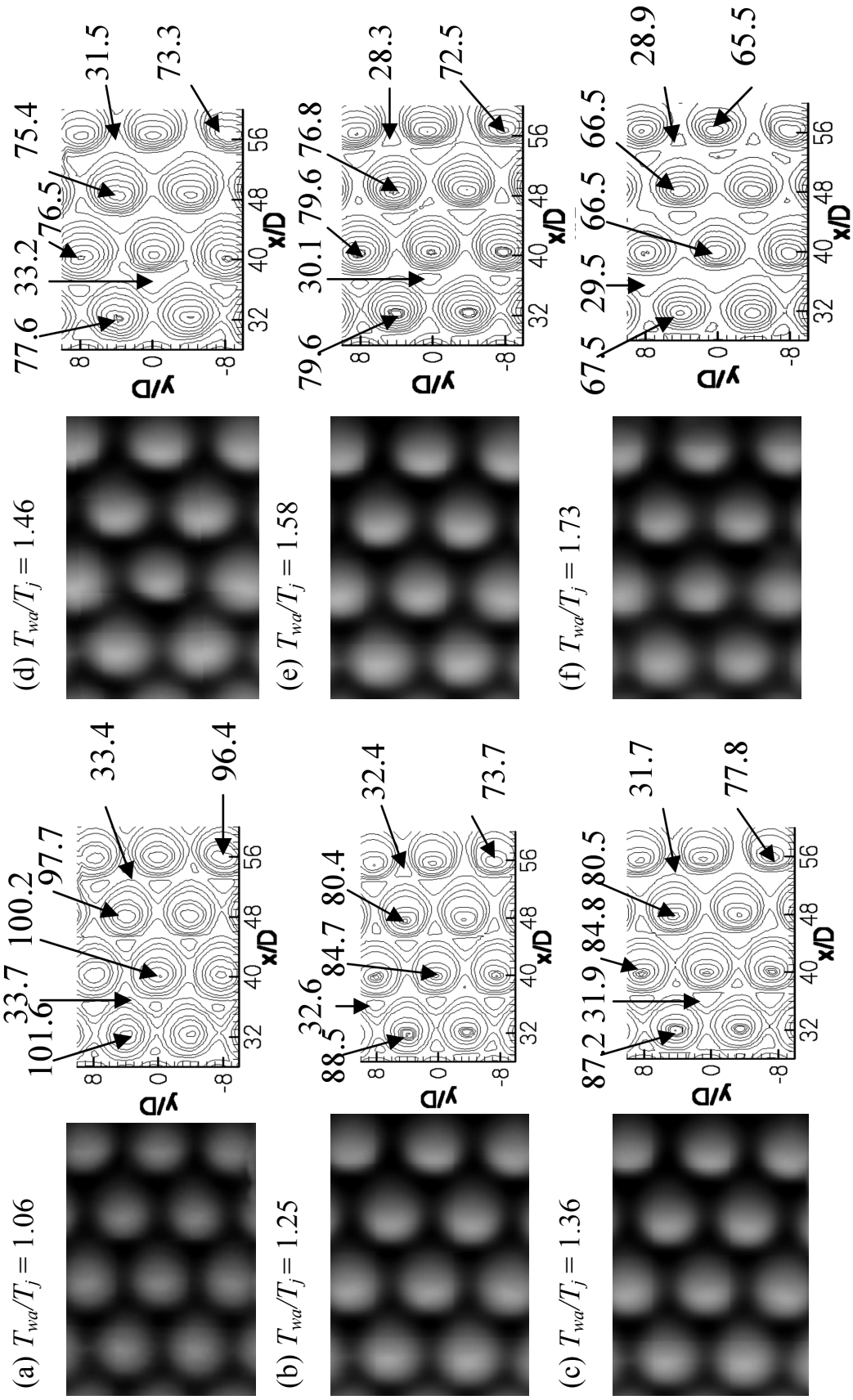


Figure 3.3. Spatially-resolved surface Nusselt number distributions for Re_j = 18000, Ma = 0.2, and T_{wa}/T_j = 1.06, 1.25, 1.36, 1.46, 1.58 and 1.73.

distribution on the target surface beneath each jet. Magnitudes of these local maximum values are about the same underneath the different impingement jets for the T_{wa}/T_j values investigated, with minor variations between streamwise rows as x/D increases. These variations with streamwise distance are further illustrated in Fig. 3.4b by local Nusselt number data as it varies with x/D for y/D = 8. They are due to the increasing effect of hot, spent air crossflow which reduces the effectiveness of the impinging jets. The smaller peak values near x/D = 32 and x/D = 48, which are positioned between the larger peak values, are due to local Nusselt number increases at spanwise locations approximately halfway between the impact points of adjacent impinging jets. Fig. 3.4a shows spanwise variations in local Nusselt number for each of the T_{wa}/T_j values and x/D = 32 with the highest Nusselt number values directly under the impingement jets. As seen in Figures 3.3, and 3.4b, Fig. 3.4a shows that local Nu values decrease as the temperature ratio increases, with the most noticeable difference a decrease in peak values.

Figure 3.5 presents Nusselt numbers for the same experimental conditions as they vary with x/D, which are line averaged over y/D from -8.0 to +8.0 (which covers two complete spanwise periods of impingement jet array geometry). Here, local maximum values are apparent, spaced approximately 8D apart, and due to the impact of impingement jets from each different streamwise row of holes. These local maximum line-averaged Nusselt number values become smaller at successive x/D locations for each value of T_{wa}/T_j temperature ratio due to the increasing crossflow effect. The oscillations in line-averaged Nusselt number are due to the high Nusselt numbers directly under impinging jets, and low Nusselt number regions between the jets. In addition to these variations, the $\overline{Nu}$ data generally decrease with T_{wa}/T_j at each x/D value.

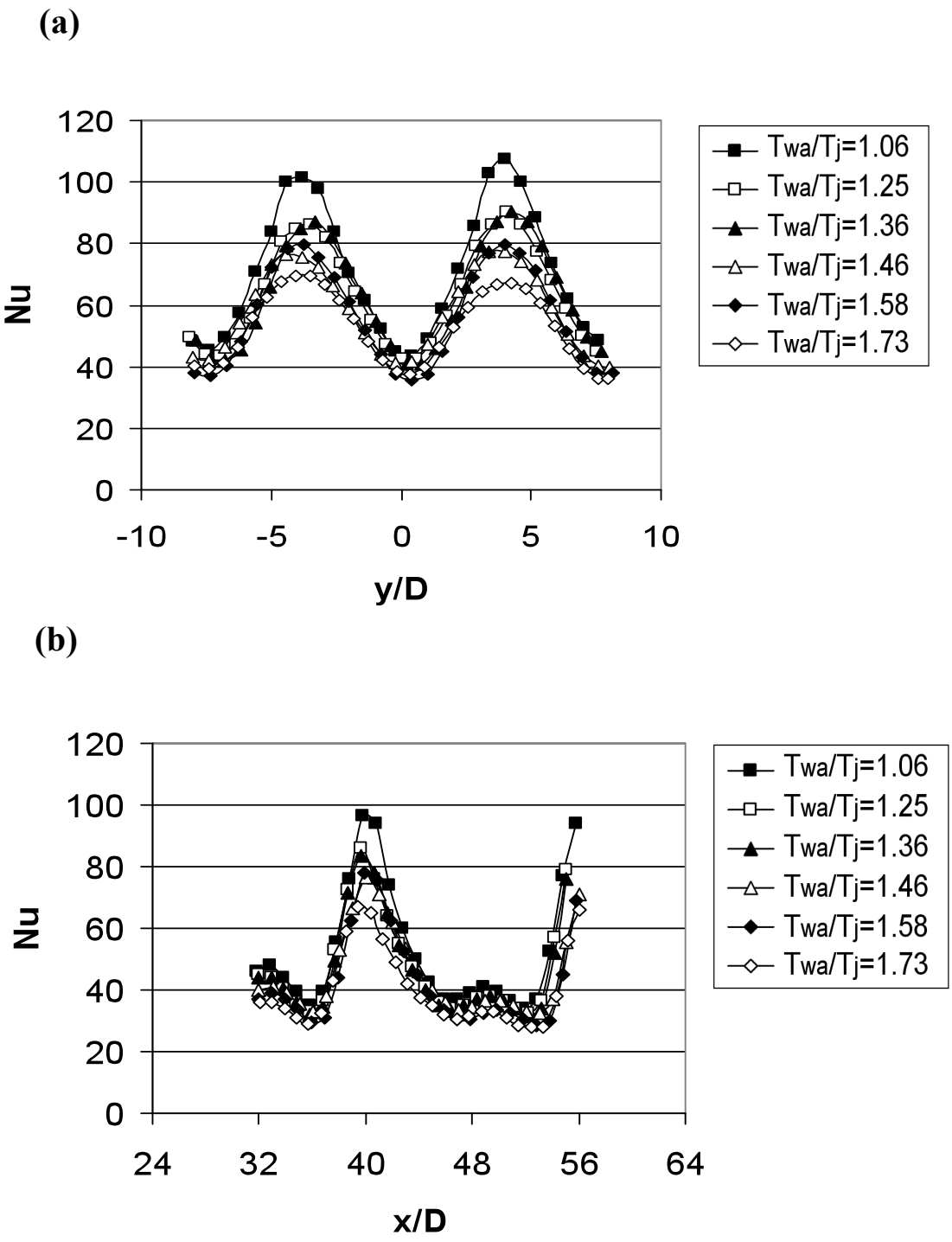


Figure 3.4. Local surface Nusselt number variations for Re_j = 18000, Ma = 0.2, and T_{wa}/T_j = 1.06, 1.25, 1.36, 1.46, 1.58 and 1.73. (a) Variations with y/D for x/D = 32. (b) Variations with x/D for y/D = 8.

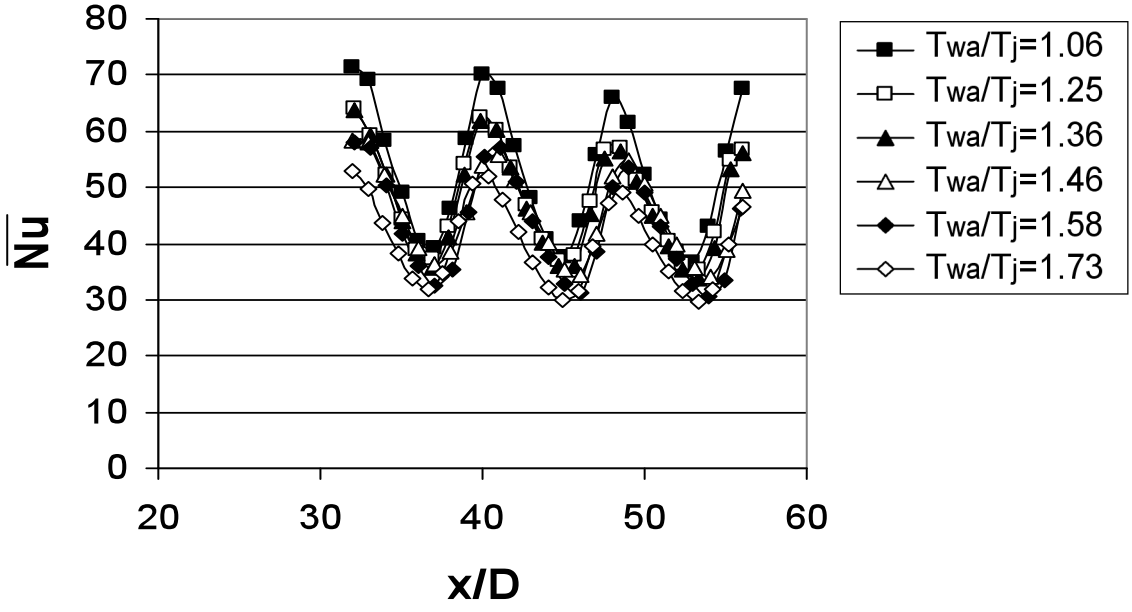


Figure 3.5. Surface Nusselt number variations with *x/D*, which are line-averaged over *y/D* from -8.0 to +8.0, for Re_j = 18000, *Ma*=0.2, and T_{wa}/T_j = 1.08, 1.25, 1.37 and 1.73.

3.4 Local area-averaged Nusselt number variations with temperature ratio

Spatially-averaged Nusselt numbers are averaged over an area that extends ±4 diameters from the specified *x/D* location and over *y/D* data points from -8 to 8. This area thus amounts to two complete spatial periods of impingement jet array geometry. Fig. 3.6 gives spatially-averaged Nusselt numbers at different values of T_{wa}/T_j, along with values from the correlation of Florscheutz et al. (1981). There are noticeable differences between the present data for T_{wa}/T_j = 1.06 and the correlation of Florscheutz et al. (1981) which is for a temperature ratio T_{wa}/T_j of approximately 1.1. The Florscheutz correlation is valid for $2500 < Re_j < 70000$, $5 < X/D < 10$, $4 < Y/D < 8$, $1 < Z/D < 3$, and $T_{wa}/T_j \sim 1.1$ for a staggered array. While the present case of Re_j = 18000, $Z/D = 3$, $X/D = 8$, and $Y/D = 8$ falls within the range specified by Florscheutz, the results indicate that the conditions appear to be beyond the range of applicability of the Florscheutz correlation. The validity of the results in the present study for temperature ratio ~1 is verified by Park et al. (2007). In both cases, spatially-averaged Nusselt number data points are given for *x/D* of 32, 40, 48, and 56. For each of these streamwise locations, the results in Fig. 3.6 show that area-averaged Nusselt numbers decrease as the T_{wa}/T_j temperature ratio increases, provided the impingement jet static temperature is held constant.

3.5 Local area-averaged Nusselt numbers and the Temperature Ratio Correlation Equation

Fig. 3.7 shows area-averaged Nusselt numbers, for particular *x/D* values, as they decrease with the T_{wa}/T_j temperature ratio for Re_j = 18,000 and $Ma = 0.2$. Here, the local area averaged Nusselt number value is determined over the area which extends at X/D = 32, 40, 48, and 56 over *y/D* from –8 to 8. The *x/D* extent for each

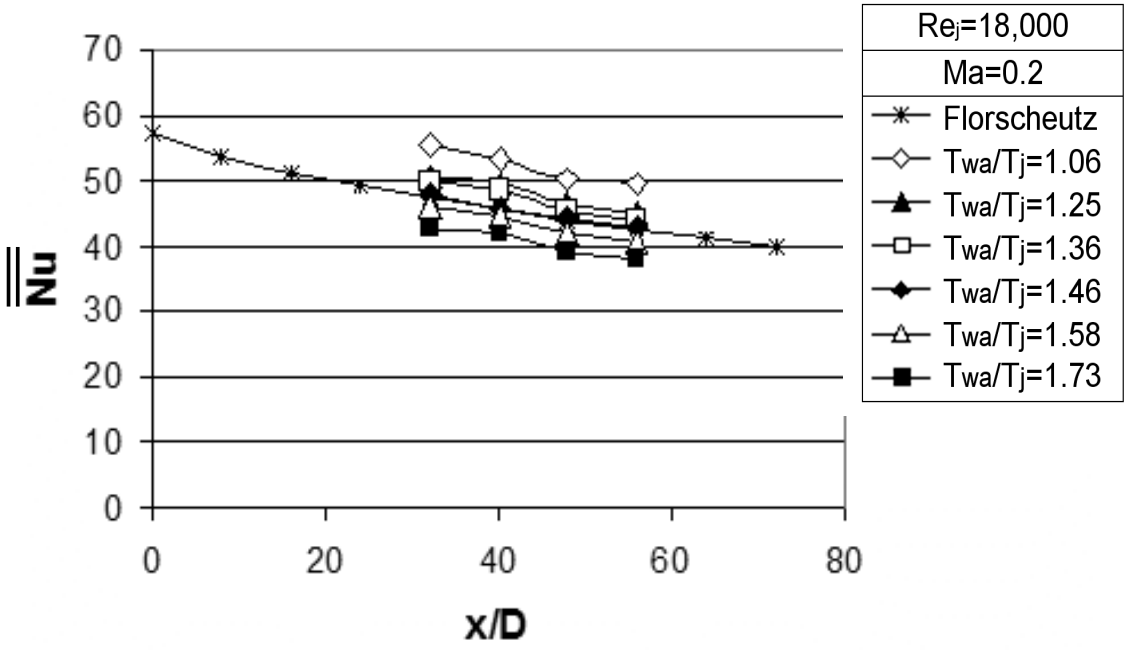


Figure 3.6. Spatially-averaged Nusselt numbers as dependent upon x/D for Re_j = 18000, Ma = 0.2, and T_{wa}/T_j = 1.06, 1.25, 1.36, 1.46, 1.58 and 1.73.

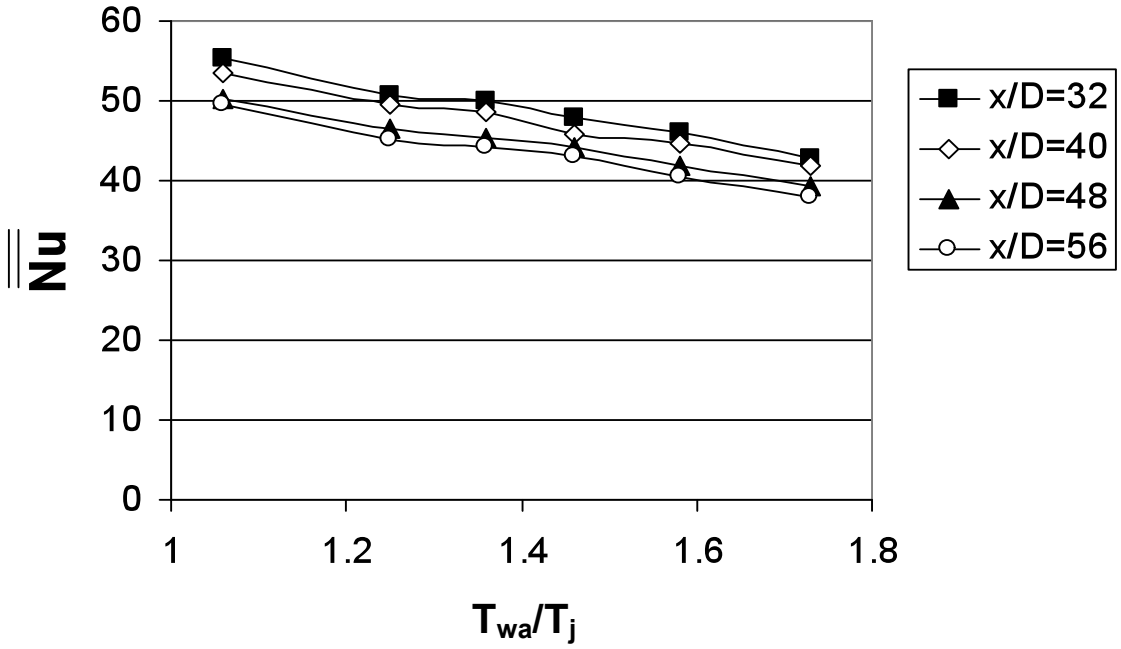


Figure 3.7. Local area averaged Nusselt numbers as dependent upon temperature ratio T_{wa}/T_j for Re_j = 18000 and Ma = 0.2.

average is ± 4 relative to the calculated value. Note that spatially-averaged target surface temperatures T_{wa} are determined over the same spatial surface areas. Nusselt number values then decrease as the T_{wa}/T_j temperature ratio increases, up to 1.73, which evidences some deterioration of impingement cooling performance. This is because the variable property effects degrade local turbulent transport. In addition, the high crossflow temperature relative to jet temperature decreases the effectiveness of the impinging jets, and causes area-averaged Nusselt numbers to decrease with x/D at each T_{wa}/T_j temperature ratio value.

Figure 3.8 shows Nusselt number ratios Nu/Nu_{cp} as they depend upon temperature ratio T_{wa}/T_j for Re_j = 18000 and Ma = 0.2. Nu_{cp} represents the constant property Nusselt number, a condition corresponding with a temperature ratio, T_{wa}/T_j, of approximately one. In the present study a temperature ratio near one (1.06) is used as an approximation for Nu_{cp}. The Nu/Nu_{cp} data in Fig. 3.8 follow the same trend as Fig. 3.7, which shows a decrease in Nusselt number as the T_{wa}/T_j temperature ratio increases from 1.06 to 1.73. The correlation equation which best represents the data in Fig. 3.8 is given by

$$\overline{\overline{Nu}}/\overline{\overline{Nu}}_{cp} = (Twa/Tj)^{-0.35} \qquad (3.1)$$

This correlation equation is determined for Re_j = 18000, Ma = 0.2, $1.06 \le T_{wa}/T_j \le 1.73$, X/D = 8, Y/D = 8, Z/D = 3, and $32 \le x/D \le 56$. However, Eq. (3.1) is expected to be valid for a wider range of incompressible (or near incompressible) flow conditions, which include Re_j from near 3,000 to about 30,000, Ma from near 0 to approximately 0.25, and a range of X/D and Y/D values in the vicinity of 8.

The Nusselt number variations which are observed as either T_{wa}/T_j or T_w/T_j varies are mostly due to variable property effects. Most important are variations of

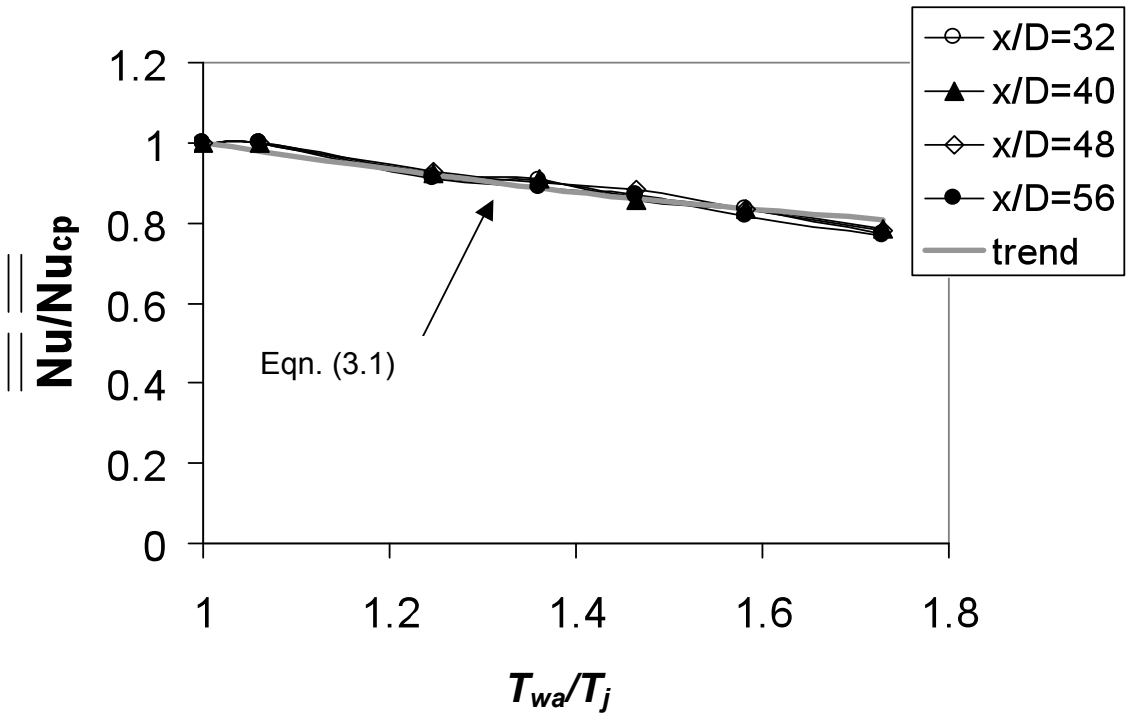


Figure 3.8. Nusselt numbers ratio data at specific x/d locations correlated with respect to temperature ratio, T_{wa}/T_j.

molecular thermal conductivity, absolute viscosity, and static density with spatial location and time, because these change as static temperature varies with spatial location and time. Note that the contributions of specific heat to Nusselt number variations are less important because its weak dependence on temperature in gas flows. The effects of conductivity, viscosity, and density variations on local turbulent trasport of momentum and heat are complex. For example, turbulent transport is generally mostly a result of mixing, collisions, and interactions between turbulent eddies of different sizes. However, ultimately, as molecular scales are approached, thermal transport is due to conduction between adjacent packets of oscillating fluid. In many cases, such molecular conduction provides some restriction on overall magnitudes of turbulent transport which can be achieved. Such limitations and the associated phenomena and interactions are especially complex in impingement array flows because they involve such a wide variety of phenomena, including jet flows, shear layer interactions, stagnation regions, interactions between adjacent impingement jets, wall-jet interactions, three-dimensional boundary layer development, and interactions between impingement jets and these boundary layers.

3.6 Summary and Conclusions

Data are provided as the ratio of impingement target plate temperature to impingement jet temperature is varied, at constant Reynolds number. The spacing between holes in the streamwise direction X is then $8D$, and the spanwise spacing between holes in a given streamwise row Y is also $8D$. The thickness of each impingement plate is $1D$, and the spacing between the hole exit planes and the target plate is denoted Z and is equal to $3D$. This impingement arrangement is similar to arrangements used in some industrial gas turbine engines, providing results and conclusions applicable to the gas turbine industry.

Local, line-averaged, and spatially-averaged Nusselt numbers decrease as the T_{wa}/T_j temperature ratio increases for any particular x/D and y/D location for Re_j = 18,000 and Ma = 0.2. The spatially-averaged Nusselt number decrease is especially substantial as the T_{wa}/T_j temperature ratio increases from 1.06 to 1.73, which evidences some deterioration of impingement cooling performance. The area beneath each impingement jet shows a higher rate of heat transfer than the surrounding areas which do not have the additional heat transfer benefit associated with perpendicular impinging jets. The effect of increasing temperature ratio is more apparent in the regions under the impinging jets where the heat transfer is noticeably reduced, a contrast from the surrounding areas, which show almost no change. This is believed to be due to variable property effects which degrade local turbulent transport in the impingement flow as T_{wa}/T_j increases. The effect of sequential streamwise rows of impingement jets is increasing amounts of crossflow, which reduce the effectiveness of downstream impingement jets resulting in a progressive decrease in local and line-averaged Nusselt numbers, regardless of the value of the T_{wa}/T_j temperature ratio. The correlation Eqn. (3.1), which gives quantitative assessment of the effects of temperature ratio on local area-averaged Nusselt numbers is expected to be valid for a range of incompressible (or near incompressible) flow conditions: $1.06 \leq T_{wa}/T_j \leq 1.73$, Z/D=3, $32 \leq x/D \leq 56$, Re_j from near 3,000 to about 30,000, Ma from near 0 to approximately 0.25, and a range of X/D and Y/D values in the vicinity of 8.

Chapter 4

Effect of Hole Spacing on Impingement Heat Transfer

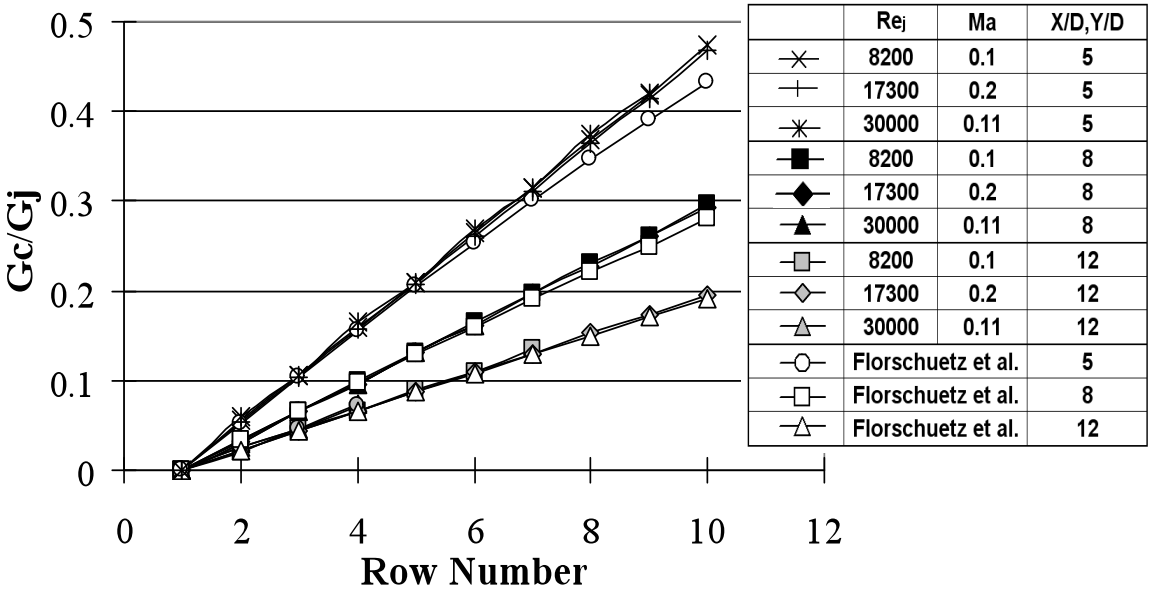
4.1 Overview

Data which illustrate the effects of hole spacing on spatially-resolved heat transfer from an array of jets impinging on a flat plate are presented. Considered are Reynolds numbers ranging from 8200 to 60,000, and Mach numbers from 0.1 to 0.2 at a temperature ratio of ~1.1. The spacing of the holes used to produce the impinging jets is 5*D*, 8*D* or 12*D* in both the streamwise and spanwise directions. Local and spatially-averaged Nusselt numbers show strong dependence on the impingement jet Reynolds number for both situations, with negligible variations between Ma = 0.1 and 0.2 at constant Reynolds number. The results of the hole spacing study are compared to the values predicted by the correlation of Florschuetz et al. (1981).

4.2 Crossflow-to-Jet Mass Flux Ratio and Discharge Coefficients

Figure 4.1a shows the ratio of crossflow mass velocity-to-jet mass velocity as it varies with *x/D* for hole spacings of 5*D*, 8*D* and 12*D*. This ratio is only as high as about 0.45 at the end of all rows of holes. Here, data from the present study show reasonably good agreement with the correlation of Florschuetz et al. (1981). Note that, *Gc/Gj* values are lower for 12*D* hole spacing than for 8*D* hole spacing, with 5*D* having the highest values when compared at a particular value of *x/D*. Discharge coefficients represent average values for all of the impingement holes on a particular test plate, and are presented in Figure 4.1b. From this graph, it is apparent that discharge coefficients decrease slightly as the Reynolds number increases.

(a)



(b)

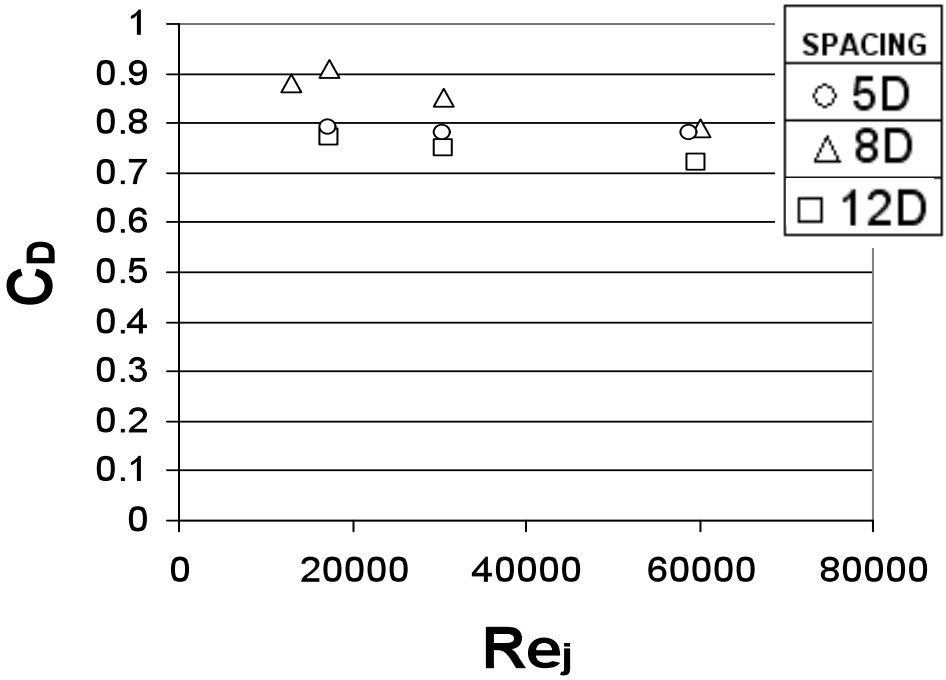


Figure 4.1. (a) Crossflow-to-jet mass velocity ratio with row number for hole spacings of 5*D*, 8*D*, and 12*D* and (b) discharge coefficient coefficient varations with Re_j for hole spacings of 5*D*, 8*D*, and 12*D* at constant Mach number 0.2.

4.3 Local surface Nusselt Number and Line-Averaged Nusselt Number Variations With Hole Spacing

Surface Nusselt number distributions are presented in Fig. 4.2 for Ma = 0.20, and Re_j = 17300, 30000, and 60000 for the three different hole spacings of 5D, 8D and 12D. The different views of the test surface are due to different infrared camera views of the target plate as different impingement plates with different Reynolds number and Mach number are employed. This is because the impingement plates which are employed are different sizes with different sizes of hole diameters. Note that, regardless of the Reynolds number and the Mach number, that the qualitative distributions of local Nusselt numbers produced by each impingement jet are similar, with good periodic repeatability in the spanwise direction for each streamwise row of impact location. Figure 4.2 also shows that local Nusselt number *peak values* for each hole spacing generally become smaller at successive x/D locations for each value of impingement jet Reynolds number and Mach number due to the detrimental effect spent air crossflow has on heat transfer. The local Nusselt number decrease with x/D for 8D hole spacing is generally more pronounced at most all x/D locations compared to the 12D hole spacing data, with the decrease even more pronounced for 5D hole spacing cases. This is a result of the cumulative effects of the interactions between adjacent jets and the resulting cross-flows for an arrangement where the jets are more closely spaced together. Figures 4.3a-f show comparisons between the different hole Reynolds numbers at constant Mach number for each of the hole spacings with local values at constant values of x/D and y/D. These comparisons each show a marked increase in Nusselt number values with increasing Reynolds number. The constant

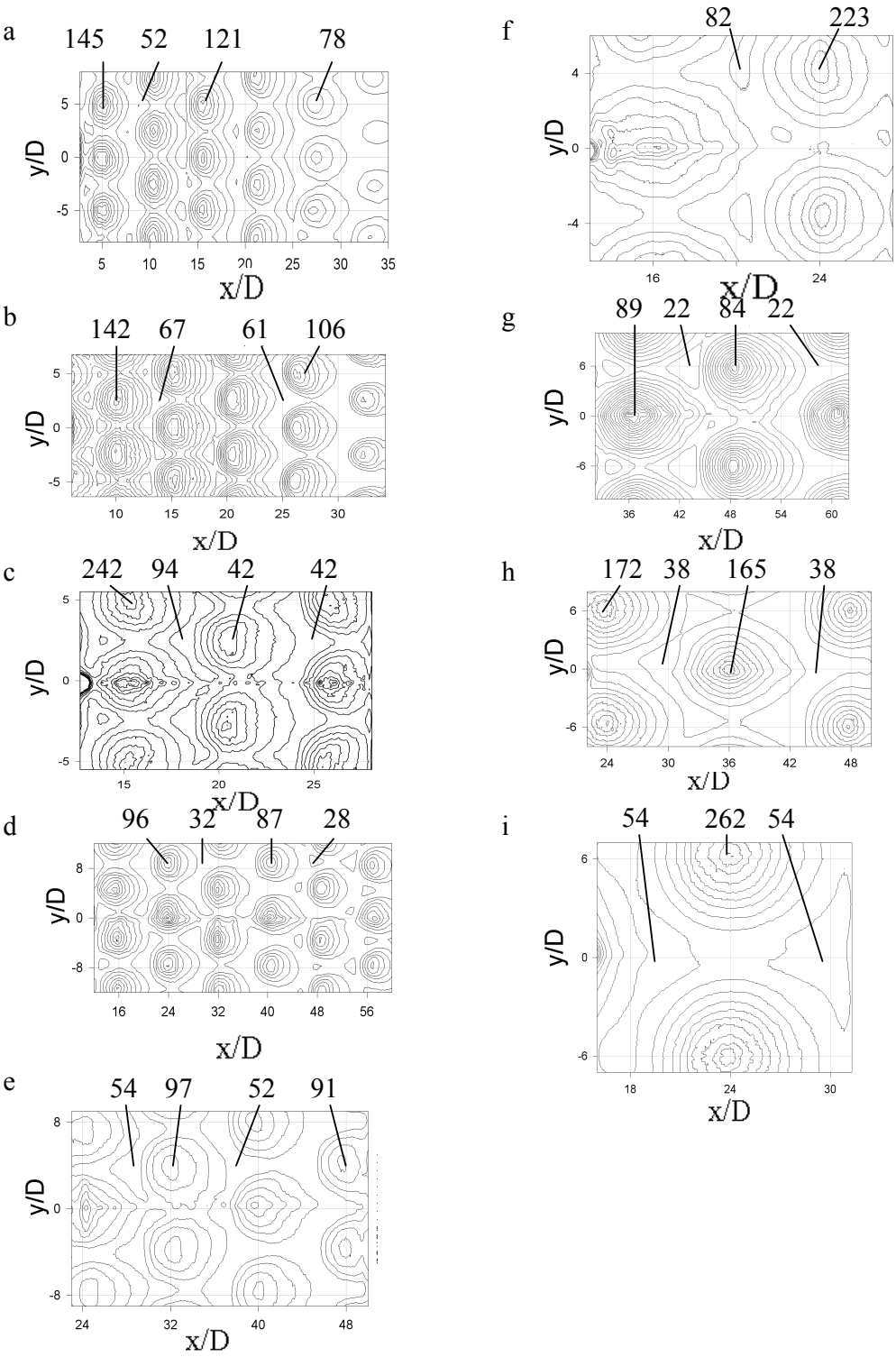


Figure 4.2. Spatially resolved distributions of surface Nusselt number for $Ma = 0.2$ with hole spacings and Re_j values of: (a) 5D and $Re_j = 17300$, (b) 5D and $Re_j = 30000$, (c) 5D and $Re_j = 60000$, (d) 8D and $Re_j = 17300$, (e) 8D and $Re_j = 30000$, (f) 8D and $Re_j = 60000$, (g) 12D and $Re_j = 17300$, (h) 12D and $Re_j = 30000$, (i) 12D and $Re_j = 60000$.

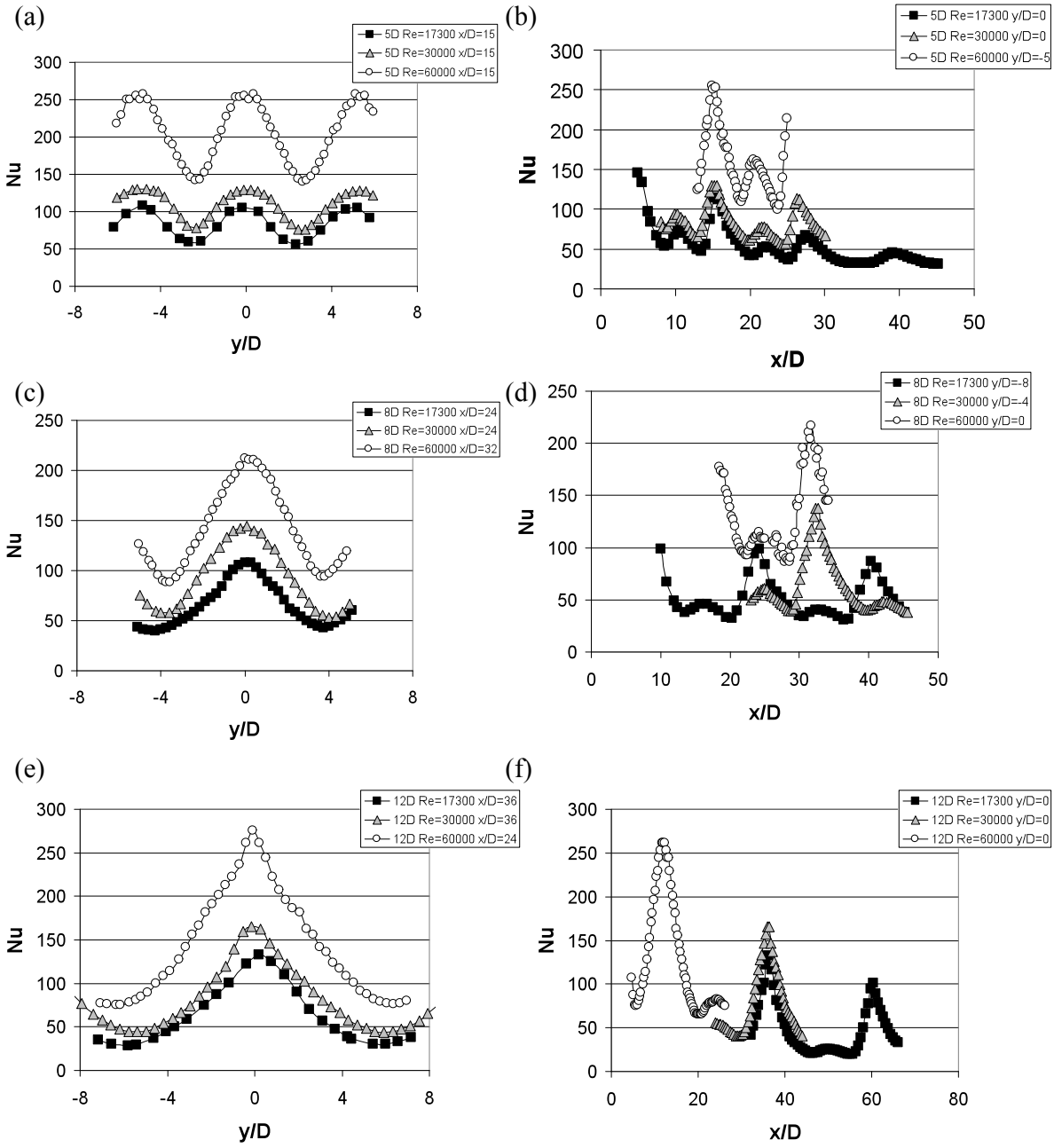


Figure 4.3. Local surface Nusselt number variations for Ma = 0.2 and Re_j values of 17300, 30000, and 60000: (a) hole spacing 5D spanwise variations, (b) hole spacing 5D lengthwise variations, (c) hole spacing 8D spanwise variations, (d) hole spacing 8D lengthwise variations, (e) hole spacing 12D spanwise variations, (f) hole spacing 12D lengthwise variations.

x/D plots show good repeatability in the spanwise direction while the constant *y/D* plots show a successive decrease in Nusselt number with increasing *x/D* due to the effects of spent air crossflow. These plots serve to better qualify the results seen in Fig. 4.2.

Figures 4.4 presents Nusselt numbers which are line-averaged over *y/D* from –2.5 to +2.5 for a hole spacing of 5*D*, from -4.0 to +4.0 for a hole spacing of 8*D*, and from -6.0 to +6.0 for a hole spacing of 12*D*. The line-averaged comparisons are at constant Mach number for each of the three hole spacings considered in the present study. Each of the three hole spacings shows considerable increase in Nusselt number with increasing Reynolds number and decreasing values with increasing *x/D*. This decrease with *x/D* is more pronounced for tighter hole spacings due to the increased effect of spent air crossflow.

4.4 Local Area-Averaged Nusselt Number Variations With Hole Spacing

Figures 4.5-4.7 compare spatially averaged Nusselt numbers for hole spacings 5D, 8D and 12D with the Florschuetz et al. (1981) correlation values. Figure 4.5 shows the comparison for 5*D* hole spacing at constant Mach number 0.20 and Re_j values of 17300, 30000, and 59000. There is good agreement between the measured values and those predicted by the correlation, with a discrepancy of between 5 and 10 percent for the lower Re_j values.

Figure 4.6 shows the comparison for 8*D* hole spacing at constant Mach number 0.20 and Re_j values of 17300, 30000, and 59000. There is good agreement between the measured values and those predicted by the correlation.

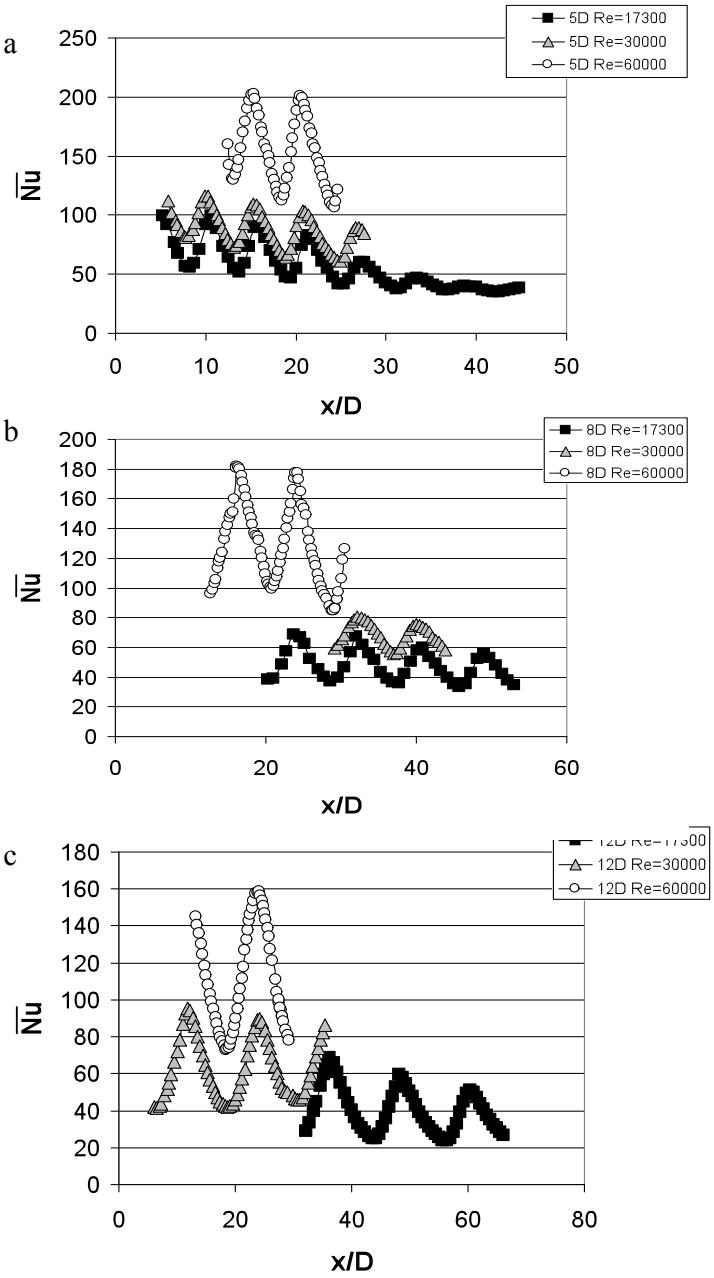


Figure 4.4. Surface Nusselt number variations which are line averaged over y/D for one hole spacing in either direction from the origin, for constant Mach number 0.20 and (a) hole spacing 5*D* Re_j = 17300, 30000, and 60000, (b) hole spacing 8*D* Re_j = 17300, 30000, and 60000, (c) hole spacing 12*D* Re_j = 17300, 30000, and 60000.

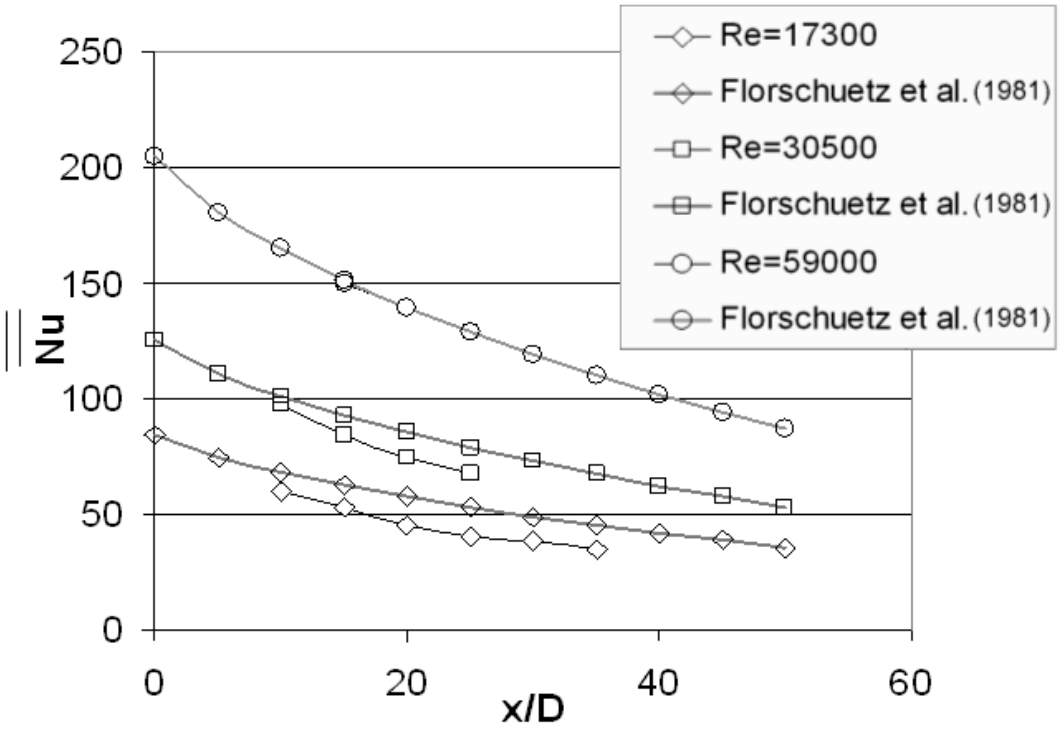


Figure 4.5. Hole spacing $X/D = Y/D = 5$ comparison of area average Nusselt numbers with correlation of Florschuetz et al. (1981) for $Ma = 0.17$, and $Re_j = 17300$, 30000, and 59000.

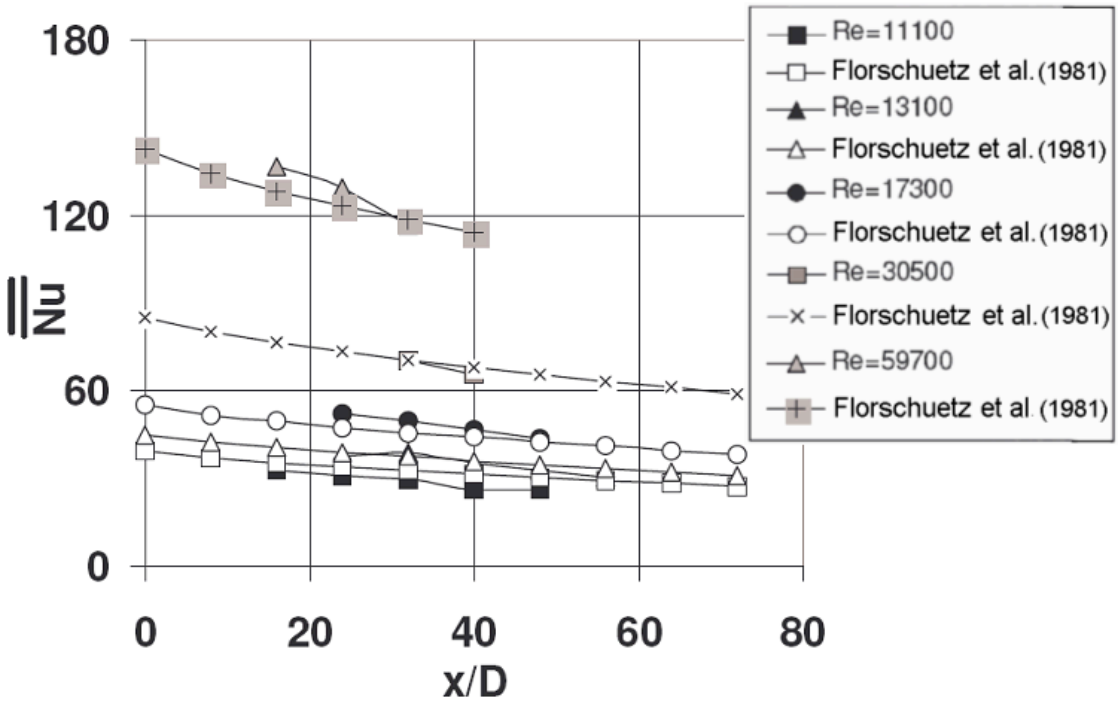


Figure 4.6. Hole spacing $X/D = Y/D = 8$ comparison of area average Nusselt numbers with correlation of Florschuetz et al. (1981) for $Ma = 0.2$, and $Re_j = 17300$, 30000, and 59000.

Figure 4.7 shows that at constant Mach number, data for hole spacing 12*D* show good agreement with the correlation predicted values for Re_j = 17300 but with values higher than predicted for higher values of Re_j.

It is of note that the 12D hole spacing data are outside the range of applicability of the Florschuetz et al. (1981) correlation, which does not consider geometries with hole spacing greater than 8*D* for a staggered array. It is therefore not surprising that these data are slightly higher than correlation predicted values.

4.5 Summary and Conclusions

Incompressible data are provided as the jet hole spacing is varied for Reynolds number values of 17300, 30000, and 30500. The spacings between holes in the streamwise direction *X* are then 5*D*, 8*D* or 12*D*, and the spanwise spacings between holes in a given streamwise row *Y* are also 5*D*, 8*D* or 12*D*. The thickness of each impingement plate is 1*D*, and the spacing between the hole exit planes and the target plate is denoted *Z* and is equal to 3*D*. These data are given for an array of impinging jets in the form of ratios of crossflow mass velocity to jet mass velocity, discharge coefficients, spatially-resolved local surface Nusselt numbers, line-averaged Nusselt numbers, and spatially-averaged Nusselt numbers.

For each of the jet spacings, local, line-averaged, and area-averaged data show strong Reynolds number dependence. Each jet produced using *X/D* = *Y/D* = 12 approximates the behaviour of an individual jet, whereas the influences of surrounding jets, including the cumulative induced cross-flows and interactions of jet-induced vortex structures, alter the effectiveness of each individual jet when *X/D* = *Y/D* = 8. The interactions between adjacent jets are still stronger for *X/D* = *Y/D* = 5. Spatially-averaged Nusselt numbers for are generally higher at closer hole spacings

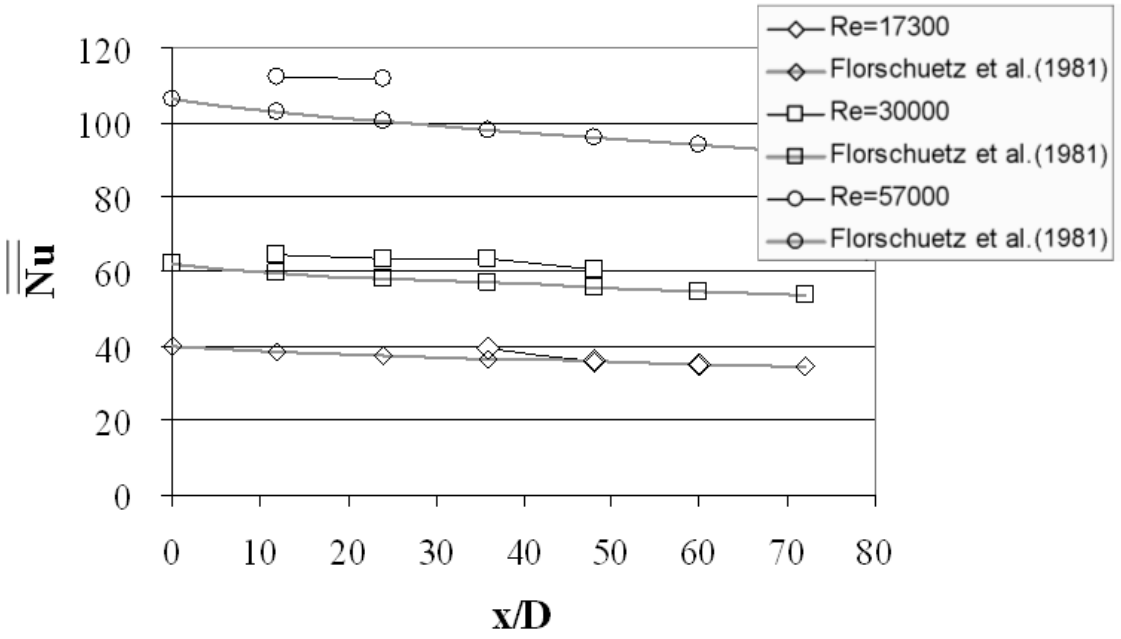


Figure 4.7. Hole spacing *X/D* = *Y/D* = 12 comparison of area average Nusselt numbers with correlation of Florschuetz et al. (1981) for *Ma* = 0.2, and Re_j = 17300, 30000, and 59000.

than values for more sparse arrays when compared at the same streamwise location. The 12*D* jet spacing data show the least variation with *x/D*, while the 5*D* jet spacing shows the most. Comparisons of periodic line-averaged Nusselt number data show that values decrease significantly at successive *x/D* locations for *X/D* = *Y/D* = 5, whereas *X/D* = *Y/D* = 12 data are approximately invariant with *x/D*. Regardless of the Reynolds number, the qualitative local Nusselt number distributions produced by different impingement jets are similar, with good periodic repeatability in the spanwise direction for each row of streamwise impact location. Crossflow mass velocity-to-jet mass velocity ratio data are lower for sparse arrays than for dense arrays when compared at a particular value of *x/D*, with reasonably good agreement with the correlation of Florschuetz et al. (1981).

Chapter 5

Effect of Compressible Flow on Impingement Heat Transfer

5.1 Overview

Data which illustrate the effects of Mach number and hole spacing on spatially-resolved heat transfer from an array of jets impinging on a flat plate are presented. Considered are Mach numbers ranging from 0.1 to 0.6. The spacing of the holes used to produce the impinging jets is 5*D*, 8*D* or 12*D* in both the streamwise and spanwise directions. Local and spatially-averaged Nusselt numbers show strong dependence on Mach number while maintaining constant Reynolds number. Hole spacing affects the Mach number effect on heat transfer, with denser arrays showing a greater increase in Nusselt number. Also included is a new correlation, based on that of Florschuetz et al. (1981), as an impingement design tool.

5.2 Local surface Nusselt Number and Line-Averaged Nusselt Number Variations With Mach Number

Figure 5.1 presents surface Nusselt number distributions for constant Reynolds number Re_j = 30000 with Mach numbers of 0.09, 0.17, 0.30, and 0.38 for hole spacing 5*D*, Mach numbers of 0.20, 0.35, and 0.45 for hole spacing 8*D*, and Mach numbers of 0.10, 0.17, 0.38, and 0.45 for hole spacing 12*D*. Figure 5.2 provides comparison plots of local data at constant x/D and y/D for each of the data sets presented in Fig. 5.1. For each of the three hole spacings there is good repeatability in the spanwise direction at every condition with decreasing *Nu* as x/D increase. This decrease is